Redirection of sphingolipid metabolism drives cytoskeletal defects in SPLIS and reveals ROCK inhibition as therapy

Adam Majcher*[1], Ranjha Khan*[2,] Kathrin Buder[3,4], Florence Bourquin[1], Julie D. Saba[2], Thorsten Hornemann[#1]

[1] Institute of Clinical Chemistry, University Hospital Zurich, Zurich, Switzerland (WAGI14, Wagistrasse 14, 8952 Schlieren, Switzerland, tel: +41 43 253 3101, a.majcher@lumc.nl, florence.bourquin@usz.ch, thorsten.hornemann@usz.ch

[2] Department of Pediatrics, University of California San Francisco, California, USA (MLK Building, University of California, San Francisco, 5700 Martin Luther King Jr. Way, Oakland, CA 94609, USA, tel: 510.414.6317, Julie.Saba@ucsf.edu, Ranjha.khan@ucsf.edu).

[3] Department of General Pediatrics and Hematology/Oncology, University Hospital Tübingen, Tübingen, Germany (Hoppe-Seyler-Strasse 1, 72076 Tübingen, Germany, tel: +49 7071 94256-0, Kathrin.Buder@med.uni-tuebingen.de)

[4] Department of Pediatric Nephrology, University Children`s Hospital Zürich, Zürich, Switzerland

* Authors contributed equally

corresponding author

Conflict of interest: Julie D. Saba is a cofounder of Sphinxion Therapeutics, Inc., which is focused on developing therapeutics for SPLIS. She is an inventor on three patents related to development of gene therapy and blood biomarkers for SPLIS. All other authors have declared that no conflict of interest exists.

Abstract:

Sphingosine-1-phosphate lyase (SPL) insufficiency syndrome (SPLIS) or nephrotic syndrome type 14 (NPHS14), is an autosomal recessive multisystem disorder caused by loss-of-function mutations in *SGPL1*, encoding the enzyme responsible for the terminal degradation of sphingosine-1-phosphate (S1P). We investigated a patient carrying a previously undescribed c.1084T>A (p.Ser362Thr) *SGPL1* variant and analyzed the metabolic and cellular consequences of SPL deficiency using patient fibroblasts, *SGPL1*-knockout HEK293T cells, and *Sgpl1*$^{-/-}$ and *Sgpl1*$^{rosa+fl/fl}$ mice. Metabolic stable isotope labelling revealed that SPL deficiency does not invariably result in S1P accumulation. Instead, SPL-deficient cells maintain near-normal S1P levels through (i) feedback regulation of de novo sphingolipid synthesis via the ORMDL–ceramide axis and (ii) increased diversion of excess ceramides into glycosphingolipids. However, perturbation of sphingolipid homeostasis—either by exogenous sphingolipid load or disruption of compensatory regulation—induces pathological intracellular S1P accumulation. In vivo, *Sgpl1*$^{-/-}$ mice exhibited pronounced urinary S1P excretion and renal S1P enrichment, accompanied by cytoskeletal disorganization and impaired epithelial morphogenesis. Mechanistically, we identify aberrant Rho–ROCK signaling as a key mediator of S1P-driven cytoskeletal dysregulation. Pharmacological ROCK inhibition with Fasudil mitigated renal cytoskeletal defects in *Sgpl1*$^{-/-}$ and *Sgpl1*$^{rosa+fl/fl}$ mice and partially restored epithelial architecture.

These findings redefine the metabolic consequences of SPL deficiency and identify S1P-driven Rho–ROCK hyperactivation as a tractable therapeutic target in SPLIS.

Introduction:

Sphingosine and its phosphorylated derivative sphingosine-1-phosphate (S1P) are critical bioactive lipids involved in numerous physiological and pathological processes.

Sphingosine-1-phosphate (S1P) is a potent lipid signaling molecule critical for regulating immune cell trafficking, vascular development, and maintaining endothelial integrity (1). S1P exerts its effects primarily through G protein-coupled receptors (S1PRs), which include five distinct subtypes (S1PR1–S1PR5), each with specific expression patterns and functions (1). In addition to its receptor-dependent actions, S1P also functions in a receptor-independent manner, influencing intracellular calcium homeostasis (2) and mitochondrial function (3). The terminal degradation of S1P is mediated by sphingosine-1-phosphate lyase (SPL), which breaks it down into a long-chain aldehyde and phosphoethanolamine (4). SPL is encoded by the *SGPL1* gene and is localized to the endoplasmic reticulum, where it catalyzes the final step in the catabolism of sphingolipids.

SPLIS or NPHS14 (also known as RENI syndrome) is a rare autosomal recessive disorder arising from biallelic mutations in *SGPL1* (5). Up to now, *SGPL1* mutations have been reported in over 76 patients (6). The disease is characterized by immunodeficiency as well as renal, neurological, skin and endocrine complications (7, 8). The overall mortality among SPLIS patients is 50%, primarily within the first decade of life, often due to end-stage kidney disease and sepsis (6).

Previous studies in cellular and mouse models have shown that SPLIS-associated SPL variants have reduced activity, which results in increased S1P levels (9-11), suggesting that an aberrant S1P metabolism might contribute to the complications in SPLIS.

Serine palmitoyl transferase (SPT) catalyzes the first and rate-limiting step of sphingolipid (SL) de novo formation, opposing SPL activity. The SPT reaction typically conjugates L-Serine and Palmitoyl-CoA, forming the sphingoid base (keto) sphinganine, which is metabolized over several steps into Ceramides (Cer) and complex sphingolipids (4, 12). In addition to *de novo* synthesis as a source of sphingolipids, cells and tissues can also absorb free and phosphorylated sphingoid bases from extracellular sources. Cellular uptake of S1P and other phosphorylated sphingoid bases requires their dephosphorylation, catalyzed by phospholipid phosphatases, followed by the passive absorption of the formed sphingosine (13).

Additionally, S1P can enter the cell through S1P receptor uptake. The resorbed sphingosine is then either reacylated to form ceramide (salvage pathway) or re-phosphorylated to S1P. Additionally, S1P is exported via sphingolipid transporter 2 (SPNS2) or by the major facilitator superfamily domain containing 2B (MFSD2B), which are expressed in different cells (14).

However, since SPL is ubiquitously expressed in all cells and tissues except erythrocytes and platelets, it is surprising that a systemic mutation in a universally active metabolic pathway manifests predominantly as a severe renal phenotype. In this study, we aimed to investigate why the reduction in SPL activity primarily affects kidney function. Specifically, we sought to identify the mechanisms that make kidney cells particularly vulnerable in SPLIS and to determine whether these underlying mechanisms can be targeted therapeutically.

Results:

A novel SPLIS-associated *SGPL1*p.(Ser362Thr) variant

An 8-week-old girl, term-firstborn of healthy Iraqi consanguineous parents (oligohydramnios, small for gestational age with birth weight of 2140 g at 37+1 gestational weeks), was diagnosed with dialysis-dependent end-stage kidney disease due to congenital nephrotic syndrome presenting with heavy proteinuria, hypalbuminemia and edema. Kidney biopsy and steroid treatment were not performed, considering the patient`s young age, which was suggestive of a genetic cause of the nephrotic syndrome. Whole exome sequencing identified a homozygous, variant in exon 12 of the *SGPL1* gene (c.1084T>A, p.Ser362Th) suspected to be pathogenic and causing SPLIS (Figure 1 B, C, D) (6). In the protein sequence, the mutation is located close to the cofactor-binding lysine at K353. Besides the renal phenotype, the patient exhibited multiple extra renal manifestations summarized in Table 1. Adrenal calcifications identified initially are shown in Figure 1. The clinical course was complicated by prolonged hospitalizations due to recurrent respiratory tract infections with global respiratory insufficiency, recurrent cytomegalovirus viremia and coagulase-negative staphylococci bacteremia, life-threatening arterial hypotension, catheter-related thromboses of several central veins of the upper thoracic aperture, increased need for peritoneal dialysis due to ultrafiltration insufficiency. At 8 months, cerebral computer tomography performed after clinical presentation of a generalized seizure, showed slightly expanded cerebrospinal fluid spaces. The patient died at the age of 9 months, most likely due to septic shock with subsequent multiorgan failure.

To investigate whether the new *SGPL1* variant was associated with changes in overall plasma SL profile, we performed an untargeted LC-MS/MS based lipidomics analysis of patient’s plasma (N=1) compared to healthy controls (N=7). In our analysis, we did not see significantly elevated S1P levels, while Cer, HexCer and SM levels were slightly increased in the patient plasma (Supplementary Figure 1). However, due to the patient's very young age and severe condition, only a limited amount of plasma was available. As a result, S1P levels were quantified from the general lipidomics analysis, which is not the best suited method to measure phosphorylated sphingoid bases. Unfortunately, there was insufficient plasma to verify S1P levels through a separate, more sensitive, targeted S1P analysis. Patient derived skin fibroblasts

showed a significant increase in S1P, Cer and HexCer while total SM was decreased (Figure 1E). However, the absolute increase in S1P was small (0.005pmol/µg protein) compared to the total differences observed for HexCer (1pmol/µg protein) or SM (2pmol/µg of protein). A similar change in the SL profile was also seen in HEK293T-*SGPL1 KO* cells (data not shown).

Downregulation of SL de-novo synthesis prevents S1P accumulation in SPL/SPL-deficient cells

SPT activity and de novo sphingolipid (SL) synthesis are regulated by ORMDL proteins (ORMDL1, ORMDL2, and ORMDL3) in response to intracellular ceramide levels (15). To see whether SL *de novo* synthesis was altered in SPL/SPL-deficient cells, we performed a stable isotope-labeling assay using d_3-^{15}N-Serine. Primary SPLIS fibroblasts as well as HEK293T *SGPL1* KO cells showed decreased SL *de novo* synthesis compared to controls. Supplementing cells with exogenous d7-sphingosine (d7-So) further reduced de novo sphingolipid (SL) synthesis in both KO and WT cells, indicating that an increase in intracellular SL levels leads to an enhanced compensatory downregulation of de novo synthesis (Figure 2B,C). After silencing ORMDL1-3 expression by siRNA we observed an increased *de novo* formation and a substantial accumulation of Sa1P and S1P (here shown as sum of both) in SPL/SPL-deficient cells (Figure 2D, Supplementary Figure 2).

In a second approach, we modulated the homeostatic control by adding fumonisin B1 (FB1), a pan-inhibitor of Ceramide Synthases 1-6 (CerS1-6) that prevents the *de novo* formation of dihydroceramide and subsequently ceramide downstream of SPT. FB1 leads to a substantial accumulation of *de novo*-formed Sa and Sa1P in *SGPL1* KO but not in WT cells (Figure 2E). This accumulation was significantly reduced when activating the inhibitory SPT subunits ORMDL1-3 with cell-permeable short-chain C6-Ceramide or by inhibiting SPT with myriocin (Figure 2F). In comparison, FB1 was significantly more toxic for *SGPL1* deficient cells compared to WT (Figure 2G). In presence of FB1, phosphorylated and non-phosphorylated LCBs increased only in SPL deficient cells (Figure 2H).

Synthesis of higher SL is an "escape" mechanism for preventing toxic S1P accumulation in SPLIS

To circumvent SPT regulation by the ORMDLs, we added isotope-labeled d7-sphinganine (d7-Sa) directly to the cells and monitored the isotopic flux. The

downstream products formed, such as d7-ceramide (d7-Cer), d7-hexosylceramide (d7-HexCer), and d7-sphingomyelin (d7-SM), showed a 3–4-fold increase (Figure 3A). Additionally, supplementation with d7-sphingosine (d7-So) or d7-sphingosine-1-phosphate (d7-S1P) at concentrations of 0.5 µM or 2.5 µM resulted in a significant increase in d7-Cer, d7-HexCer, d7-SM, and d7-S1P levels (Figure 3B). Total sphingolipid (SL) levels were calculated as the sum of all non-labeled and M+7-labeled SL species. Overall, SPLIS primary fibroblasts, *HEK293T SGPL1* KO cells, and HK2 *SGPL1* KO cells exhibited elevated SL levels compared to WT cells. Notably, in addition to S1P, ceramide (Cer) and hexosylceramide (HexCer) levels were predominantly increased, while total sphingomyelin (SM) levels showed minimal changes (Figures 3D and 3E). Total S1P levels were elevated in all three KO cell lines. However, all KO cell lines accumulated substantial amounts of HexCer (depicted in blue in Figures 3C, D, and E). To assess whether the conversion of excess SLs to HexCer is crucial for maintaining SL homeostasis and avoiding toxic SL accumulation in SPLIS, we incubated WT and *SGPL1* KO cells with increasing concentrations of sphingosine (So) in the presence of a glucosylceramide synthase (GCS) inhibitor (Genz-123346). Blocking GCS indeed sensitized *SGPL1* KO cells to So toxicity, indicating that the conversion of excess SLs into HexCer serve as a metabolic escape mechanism to prevent toxic S1P accumulation (Figure 3F).

SPLIS-inducing variants of *SGPL1* diminished the cellular ability to clear excess S1Ps

SPL converts sphingosine-1-phosphate (S1P) into hexadecenal and phosphoethanolamine. Hexadecenal is further oxidized by aldehyde dehydrogenase 3A2 (ALDH3A2) into a fatty acid, which is subsequently metabolized into other lipids, including glycerophospholipids such as phosphatidylcholine (PC) (Figure 4A) (16). Increasing concentrations of supplemented d7-sphinganine (d7-Sa) correlated with the formation of d7-labeled PCs in WT cells. This conversion was absent in *SGPL1* KO cells, which instead showed a marked accumulation of d7-S1P (Figure 4B). Additionally, other d7-labeled downstream phospholipids, such as d7-phosphatidylethanolamines (d7-PEs), d7-triglycerides (d7-TGs), and d7-diacylglycerols (d7-DGs), were detected (data not shown). Similarly, when primary SPLIS fibroblasts were supplemented with either d7-sphingosine (d7-So) or d7-S1P, WT cells efficiently converted the labeled SL into d7-PC. In contrast, SPLIS fibroblasts

primarily converted the labeled SL into d7-S1P, with minimal formation of d7-PC (Figure 4C).

Different SPLIS mutations are associated with varying disease severities. To investigate this, we compared the activity of six *SGPL1* variants by expressing them in *HEK293T SGPL1* KO cells (Figure 4D) and analyzing their ability to convert d7-Sa into d7-PC. All disease-associated variants demonstrated a reduced capacity to degrade d7-S1P and to form d7-PC. Notably, the most prevalent SPLIS variant, p.Arg222Gln (6), exhibited the highest residual activity (approximately 10%) and the highest protein expression (Supplementary Figure 2B, Supplementary Figure 3).

Sgpl1 KO mice accumulate large quantities of S1P in kidneys and urine

SPL deficiency results in an inability to efficiently clear exogenously supplemented sphingolipids (SL). Intracellularly, S1P levels are typically maintained in the nanomolar range, while S1P is highly abundant in plasma (~0.5 µM). Since the kidneys process large volumes of blood, they are consistently exposed to high levels of extracellular S1P. To prevent toxic intracellular accumulation of S1P, kidney cells must actively degrade this metabolite.

Sgpl1$^{-/-}$ mice develop nephrosis characterized by hypoalbuminemia and an elevated urine albumin-to-creatinine ratio, mirroring the pathology observed in humans. We analyzed total S1P content in the kidney, liver, and muscle of WT, *Sgpl1*$^{+/-}$, and *Sgpl1*$^{-/-}$ mice. Compared to WT animals, *Sgpl1*$^{-/-}$ mice showed increased S1P levels in tissues and urine (Figures 5A–D). The most pronounced S1P accumulation was observed in the kidneys of *Sgpl1*$^{-/-}$ mice, which is the primary organ affected in SPLIS. Glomerulosclerosis in these mice was confirmed histologically (Figure 5E). In contrast, heterozygous *Sgpl1*$^{+/-}$ mice did not exhibit significant S1P accumulation, suggesting that a single functional allele is sufficient to maintain normal S1P levels.

The uptake of extracellular sphingoid bases is toxic to *Sgpl1*-KO cells (Figure 3F). We hypothesize that a similar mechanism underlies the specific nephrotoxic effects seen in SPLIS. Kidney cells of *Sgpl1*$^{-/-}$ mice absorb S1P from plasma and urine but are unable to degrade the intracellular excess of SL. The kidney contains many highly specialized cell types, some of which may be particularly vulnerable to the toxic effects of S1P due to their exposure to both excreted and reabsorbed lipids in SPLIS patients.

Intracellular accumulation of S1P causes transient cell contraction in SPLIS fibroblasts

Exogenous supplementation with sphingosine (So) or S1P leads to intracellular S1P accumulation in SPL-deficient cells (Figure 3). This increase in intracellular S1P is associated with a transient cell-rounding phenotype in SPLIS fibroblasts. Approximately 6–12 hours after the addition of So or S1P, the cells contract and subsequently re-flatten after 24 hours. This behavior was not observed in control fibroblasts (Figures 6A, B, and C).

We compared the kinetics of So and S1P absorption from the medium and the resulting intracellular S1P accumulation. Cells were incubated with d7-So or d7-S1P for 0, 16, and 40 hours. Both lipids were effectively absorbed and cleared from the medium within 24 hours at similar rates (Figure 6D). We did not detect d7-S1P release into the medium, indicating that the absorbed lipids were primarily metabolized intracellularly. In d7-So-treated SPLIS fibroblasts, intracellular d7-S1P levels increased transiently during the first 16 hours and returned to baseline by 40 hours (Figure 6E). This transient rise in intracellular S1P was closely associated with the rounding phenotype in SPLIS cells, but not in WT fibroblasts. A similar kinetic profile was observed when supplementing d7-S1P (Figure 6F).

These findings suggest that the transient rise in intracellular S1P influences the cytoskeletal dynamics of the cells, which may be relevant to the pathogenesis of SPLIS. In fact, supplementation with S1P or So in a cell migration assay confirmed the transient contraction phenotype, with re-flattening after 24 hours coinciding with the initiation of cell migration. Control fibroblasts did not show this behavior (Extended Figure 6A).

The addition of FB1 caused an increase in Sa1P levels in SPLIS fibroblasts (Figure 2E), leading to progressive cell rounding and eventual cell death, while control fibroblasts remained unaffected. This FB1-induced phenotype was rescued by co-treatment with the SPT inhibitor Myriocin, supporting the notion that the toxic response to FB1 is a consequence of de novo SL synthesis (Extended Figure 6B).

Inhibiting ROCK prevents cytoskeletal changes in SPLIS fibroblasts and a *SGPL1*-deficient HK2 cell line

S1P signals through five G-protein-coupled sphingosine-1-phosphate receptors (S1PR1–5), with S1PR2 playing a crucial role in cytoskeletal regulation. Upon S1P

binding, S1PR2 activates the Rho-associated coiled-coil-containing protein kinase (ROCK) pathway, which promotes actin stress fiber assembly and focal adhesion formation. These processes are essential for maintaining cell shape, motility, and stability. To determine whether the observed cytoskeletal effects of S1P in SPLIS fibroblasts are linked to this pathway, we inhibited ROCK using the specific inhibitor fasudil. Additionally, we compared the effects of Fingolimod (FTY720), an antagonist of S1PR1, 3, 4, and 5 (but not S1PR2), and JTE013, a specific S1PR2 antagonist (17). The contraction phenotype was assessed in an *SGPL1*-deficient human proximal tubule cell line (HK2) using phalloidin staining (Figure 7). Inhibiting the Rho-ROCK axis with fasudil prevented the contraction phenotype in SPLIS cells. JTE013 showed a partial rescue effect, while FTY720 had no effect, indicating that S1PR2 is responsible for the contraction phenotype. For quantitative analysis, we used the software tool CellProfiler. Cell contraction was quantified per cell and defined by the function $1/\log_{10}$(Cell surface/Nucleus surface). Averages from four images per well were used for the analysis. SPLIS fibroblasts exhibited significantly increased cell rounding in response to S1P treatment, which was reduced in the presence of fasudil (Figure 7B). Finally, we tested the effect of fasudil on HK2 kidney cells. *SGPL1* KO or WT HK2 cells were cultured with increasing concentrations of S1P in the presence or absence of fasudil. In *SGPL1* KO HK2 cells, S1P disrupted the formation of a coherent epithelial layer, a defect that was reversed when fasudil was co-administered (Figure 7C). In summary, these findings suggest that inhibition of the Rho-ROCK signaling axis can rescue SPLIS-induced cytoskeletal phenotypes.

Fasudil ameliorates renal dysfunction and structural damage in SPL deficient mice

To test whether inhibition of the Rho–ROCK pathway can also improve renal pathology *in vivo*, we treated inducible *Sgpl1*-deficient mice (*Sgpl1*$^{rosa+fl/fl}$) with the ROCK inhibitor fasudil. Successful deletion of *SGPL1* in kidney tissue after tamoxifen induction was confirmed by immunoblotting (Figure 8A). As expected, untreated *Sgpl1*$^{rosa+fl/fl}$ mice developed a pronounced nephrotic phenotype, characterized by a strong increase in the urinary albumin-to-creatinine ratio (ACR), reduced serum albumin levels, and elevated serum creatinine and blood urea nitrogen (BUN), indicating impaired glomerular filtration and renal failure (Figure 8B–D).

Importantly, fasudil treatment significantly improved all major functional parameters of nephrosis in *Sgpl1*$^{rosa+fl/fl}$ mice. Urinary ACR was markedly reduced in fasudil-treated *Sgpl1*$^{rosa+fl/fl}$ mice compared with untreated knockouts, indicating a substantial attenuation of glomerular barrier dysfunction (Figure 8B). In parallel, serum albumin levels were partially restored, while serum creatinine and BUN concentrations were significantly decreased, reflecting an improvement of global renal function (Figure 8C–D). Histopathological analysis further supported the functional data. Periodic acid-Schiff (PAS) staining of kidney sections revealed severe glomerular damage in untreated *Sgpl1*$^{rosa+fl/fl}$ mice, including mesangial expansion, glomerular hypercellularity, and protein casts, whereas fasudil-treated *Sgpl1*$^{rosa+fl/fl}$ mice displayed a markedly improved glomerular architecture with strongly reduced structural abnormalities (Figure 8G–I). The glomerulosclerosis was significantly reduced in the fasudil treated mice (Figure 8J).

At the cytoskeletal level, phalloidin and WT1 co-staining demonstrated a severe loss of organized F-actin structures in glomeruli of untreated *Sgpl1*$^{-/-}$ mice. In contrast, fasudil treatment restored prominent F-actin signals within WT1-positive glomeruli, indicating recovery of podocyte cytoskeletal organization (Figure 9). Together, these data demonstrate that ROCK inhibition by fasudil significantly improves both functional and structural manifestations of nephropathy in SPL-deficient mice.

Discussion:

SPLIS, or nephrotic syndrome type 14, is an inherited disease caused by recessive mutations in *SGPL1*. Since SPL is responsible for the terminal degradation of sphingolipids (SL), reduced SPL activity is expected to result in increased intracellular SL levels. However, the underlying metabolic rearrangements caused by SPL insufficiency remain poorly understood. Additionally, the pathophysiological mechanisms of SPLIS leading to nephrosis are not well characterized. Here, we report the case of a patient with a novel SPLIS-associated *SGPL1* variant (*p.Ser362Thr*). The patient presented with congenital nephrotic syndrome and immunodeficiency, resulting in early death at 9 months of age. Contrary to previous studies (18), we did not observe significantly increased S1P levels in the patient's plasma and found only slightly elevated intracellular S1P levels in patient-derived skin fibroblasts. Instead, we detected substantially increased levels of ceramide (Cer), sphingomyelin (SM), and hexosylceramide (HexCer) (Supplementary Figure 1)

However, circulating S1P levels can be suppressed during acute critical illness. Systemic inflammation such as sepsis is associated with reductions in plasma S1P (19), indicating that severe illness could mask genotype-specific effects. As the patient carrying the S362T mutation was critically ill at the time of sampling, the measured plasma S1P concentrations may therefore underestimate the mutation-related metabolic disturbance. Due to the young age and critical condition of the patient, only very little plasma was available, and the lipid extraction methodology we used was developed for a general lipidomics analysis and not optimized for S1P recovery.

Sphingolipid (SL) de novo formation is initiated by serine palmitoyltransferase (SPT) and regulated by its subunits ORMDL1-3 in response to intracellular ceramide levels (20, 21). Increasing intracellular SL content by supplementing sphingosine, sphinganine, or membrane-permeable C6-ceramide reduced SPT activity and lowered SL de novo synthesis in both WT and SPL-deficient cells (15). In fact, SPT activity and SL de novo synthesis are markedly reduced in SPL-deficient cells, including patient-derived fibroblasts. Reduced SPT activity has also been reported in SPL-deficient neurons (22). We hypothesize that in SPLIS, the impaired breakdown of SL is partially offset by a decrease in SL *de-novo* synthesis, thereby helping to maintain low intracellular S1P levels despite the absence of SPL activity. In contrast, inhibiting ceramide synthesis with FB1 or lowering ORMDL1-3 expression, significantly increases SPT activity. Under conditions of increased SL synthesis, SPL-deficient cells accumulated significant amounts of S1P, which was not observed in cells expressing functional SPL. Conversely, S1P accumulation was prevented when C6-ceramide was supplemented in addition to FB1. These findings suggest that in the absence of SPL, SPT regulation via the ceramide-ORMDL axis is crucial for maintaining baseline SL levels. This hypothesis is supported by data from *Drosophila*, where the muscle phenotypes in flies with hypomorphic mutations in *Sply* (the fly orthologue of SPL) were attenuated by crossing in a hypomorphic mutant of *lace* (the orthologue of SPT) (23). The importance of controlling SPT and SL- *de novo* synthesis in absence of SPL activity is further supported by the higher toxicity of FB1 in SPL-deficient cells (Figure 2G). Typically, we did not observe a significant increase in intracellular S1P or a notable release of S1P into the medium in the absence of SPL (Figure 6D). However, we observed a significant increase in hexosylceramide (HexCer), suggesting that the increased synthesis of glycosphingolipids may serve as a secondary compensatory

mechanism to prevent intracellular accumulation of S1P and other potentially harmful SL species. This protective mechanism might explain why supplementing low amounts of d7-Sa to SPL-deficient cells increased HexCer levels without altering S1P, while higher concentrations of d7-Sa overloaded the system's compensatory capacity, resulting in a toxic increase in S1P. A compensatory conversion of ceramide into HexCer has also been reported in SPL-deficient neurons (22). SPL-deficient cells supplemented with external SL exhibited the highest HexCer levels. However, blocking HexCer synthesis with the glucosylceramide synthase (GCS) inhibitor *Genz-123346* sensitized SPL-deficient cells to sphingosine supplementation, further supporting the role of HexCer synthesis as a compensatory mechanism.

SPL converts S1P into fatty aldehydes, which are subsequently metabolized into fatty acids and ultimately incorporated into glycerophospholipids (e.g. PCs PEs) and neutral lipids (e.g. TGs and DGs) (16). In *SGPL1*-deficient cells, the inability to efficiently cleave S1P, results in reduced conversion into glycerophospholipids, particularly when cells are supplemented with external LCBs such as d7-So, d7-Sa or d7-S1P (Figure 4). This impaired conversion has been linked to reduced PE formation in SPLIS, which may compromise autophagy, as lipidation of LC3—a key step in autophagosome formation—relies on adequate PE levels (24).

The SPLIS variants of SPL reduce enzyme activity (Figure 4D) which affects the conversion of externally supplemented SL into PCs (Figure 4D). The highest residual activity was observed for *SGPL1* p.Arg222Gln, which is the most frequently reported SPLIS variant and is associated with a comparatively mild phenotype (7) (6).

We observed significant accumulation of S1P in the tissues, blood, and urine of *Sgpl1*$^{-/-}$ mice. The most pronounced S1P accumulation was in the kidneys, the primary organ affected in SPLIS. Kidneys are constantly exposed to relatively high S1P concentrations in the blood (approximately 0.5 µM), creating persistent pressure to degrade the reabsorbed S1P. Elevated S1P levels in the urine of *Sgpl1*$^{-/-}$ mice suggest that in SPLIS, tubular kidney cells exposed to high extracellular S1P levels, but incapable of degrading it, may be particularly vulnerable to its toxic effects. Given that S1P reabsorption from urine is specific to the kidneys, this inability to degrade S1P likely explains the selective nephrotic phenotype observed in SPLIS.

The supplementation of external sphingolipids (So or S1P) to SPLIS primary fibroblasts caused profound cytoskeletal changes, manifesting as a time-dependent

but transient cell contraction closely correlated with changes in intracellular S1P levels. Similarly, supplementation of S1P induced epithelial defects in SPL-deficient HK2 cells. S1P is a pharmacologically potent molecule that exerts its effects through five specific receptors (S1PR1–5) (25). S1PR2 links to cytoskeletal regulation via the Rho/ROCK signaling pathway (26) and altered S1PR2 signaling has been linked to kidney disease previously (27). Blocking S1PR2 with JTE013 and inhibiting the ROCK signaling axis with fasudil prevented S1P-induced cytoskeletal changes in SPLIS primary fibroblasts and *HK2 SGPL1* KO cells.

Our in vivo data now provide direct functional and structural evidence that pharmacological inhibition of the Rho–ROCK signalling axis can significantly attenuate nephropathy in *SGPL1* deficiency. Treatment of inducible *Sgpl1*-deficient mice with the ROCK inhibitor fasudil resulted in a marked improvement of classical nephrotic parameters, including a substantial reduction of albuminuria, partial normalization of serum albumin levels, and significant decreases in serum creatinine and blood urea nitrogen. These findings demonstrate that ROCK inhibition improves glomerular barrier function and global renal performance in the context of *SGPL1* deficiency.

Histopathological analysis further corroborated the functional rescue. Untreated *Sgpl1*-deficient mice exhibited severe glomerular pathology characterized by mesangial expansion, hypercellularity, and protein casts, consistent with progressive glomerulosclerosis. In contrast, fasudil-treated animals displayed preserved glomerular architecture with a strong reduction of these pathological features. At the cellular level, phalloidin and WT1 co-staining revealed that the profound loss of organized F-actin structures in podocytes of untreated *Sgpl1*-deficient mice was largely reversed by fasudil treatment, indicating restoration of podocyte cytoskeletal integrity.

These in vivo findings strongly support our cellular data and the model in which pathological intracellular accumulation of S1P in *SGPL1*-deficient renal cells activates S1PR2–Rho–ROCK signalling, leading to actin cytoskeletal destabilization, podocyte dysfunction, and breakdown of the glomerular filtration barrier. However, the upstream link between elevated intracellular S1P and Rho–ROCK activation in SPLIS remains unclear. One possibility is that excess S1P is exported and activates S1PR2/3, which couple to G12/13–RhoA. Alternatively, intracellular S1P may affect Rho regulators directly, without involving surface receptors. The fact that ROCK inhibition restores

both cytoskeletal organization and renal function identifies this pathway as a central downstream effector of S1P toxicity in SPLIS. This is fully consistent with previous work linking aberrant Rho–ROCK signalling to proteinuric kidney disease, podocyte effacement, and progressive glomerulosclerosis in other pathological settings.

From a translational perspective, these results are highly relevant. Fasudil is already clinically approved and has a well-established safety profile, making ROCK inhibition an immediately actionable therapeutic concept for SPLIS, a disease for which no targeted treatment currently exists. Importantly, ROCK inhibition targets a downstream pathogenic signalling mechanism rather than the sphingolipid metabolic defect itself. This may avoid the inherent risks of metabolic substrate-reduction strategies, such as induction of alanine-driven deoxy-sphingolipid formation or unintended consequences of broadly suppressing sphingolipid biosynthesis.

However, Fasudil does not correct the underlying inability to degrade S1P, and therefore likely acts by blocking a key toxic signalling axis rather than eliminating the primary metabolic trigger. Long-term efficacy, optimal dosing regimens, and potential off-target effects in the setting of chronic SPLIS will require further investigation. In addition, it will be important to determine whether ROCK inhibition can also mitigate extra-renal manifestations of SPLIS, including neurological and immunological complications.

In conclusion, our data identify the Rho–ROCK pathway as a central effector of S1P-driven nephrotoxicity in *SGPL1* deficiency and establish pharmacological ROCK inhibition as a highly promising therapeutic strategy for SPLIS-associated nephropathy.

Methods:

Sex as a biological variant

The patient sample was from a female individual. The animal experiments were performed in mixed-sex groups. We did not observe any overt sex-dependent differences.

Cell culture

HEK293T cell lines and primary fibroblasts were grown in high-glucose DMEM (Thermo Fisher Scientific) supplemented with 10% fetal bovine serum (FBS) and 1%

Penicillin/Streptomycin (P/S) in a 5% CO_2 incubator at 37°C. Primary skin fibroblasts were isolated from patient and healthy control skin biopsies. HK2 cell lines were grown in DMEM/F-12 (Thermo Fisher Scientific) supplemented with 10% fetal bovine serum (FBS) and 1% penicillin-streptomycin (P/S) in a 5% CO_2 incubator at 37°C. For the fluorescence microscopy experiments, cells were grown in DMEM without phenol red supplemented with 10% fetal bovine serum (FBS) and 1% P/S in a 5% CO_2 incubator at 37°C. For the transfection and silencing experiments, cells were grown in high-glucose DMEM supplemented with 10% fetal bovine serum (FBS) without any addition of P/S. Cells were tested for mycoplasma contamination.

SGPL1 KO cell lines

HEK293T *SGPL1* KO cell line was a gift from Dr. Par Haberkant and generated using CRISPR/Cas 9 as described before (28).

Kidney proximal tubule cell line (HK2) *SGPL1* KO cell line was a gift from Dr. Robert Engel and generated using CRISPR/Cas9 as described before (29).

Plasmids generation

Wild type *SGPL1* was cloned into the p.Lenti-V5 vector (V498–10, Thermo Fisher Scientific), and PCR-based site-directed mutagenesis was used to introduce SPLIS-associated *SGPL1* mutations using primers shown in Table 2, following manufacturer's recommendation (Invitrogen). Generated plasmids were confirmed by Sanger sequencing.

Generation of the *SGPL1* point mutant cell lines

HEK293T *SGPL1* KO cell lines were transfected with P.Lenti-V5 Plasmid expressing WT *SGPL1* or *SGPL1* missense variants using Lipofectamine 3000 (L3000001, Thermo Fisher Scientific). pLenti-V5 containing beta-Galactosidase (V498–10, Thermo Fisher Scientific) was used as an empty vector control. Transfected cells were selected by culturing in DMEM media (10% FBS) with Blasticidine (A1113903, Thermo Fisher Scientific, 20µg/mL) for 4 weeks.

Primers:

Mutation	Primer Sequence

SGPL1 Arg222Gln_F	5'-AAA GCA TAT CAG GAT CTG GCC TTT GAG AAG GGG ATC AAA AC-3'
SGPL1 Arg222Gln_R	5'-AGG CCA GAT CCT GAT ATG CTT TGC AGG CCA TCA GTA TGC-3
SGPL1 Arg222Trp_F	5'-AAA GCA TAT TGG GAT CTG GCC TTT GAG AAG GGG ATC AAA AC-3'
SGPL1 Arg222Trp_R	5'-AGG CCA GAT CCC AAT ATG CTT TGC AGG CCA TCA GTA TGC-3'
SGPL1 Ser346Ile_F	5'-AGG TGT AAC CAT CAT TTC AGC TGA CAC CCA TAA GTA TGG C-3'
SGPL1 Ser346Ile_R	5'-CAG CTG AAA TGA TGG TTA CAC CTT TCA CCC GGA AAT C-3'
SGPL1 Gly360Val_F	5'-TGC CCC AAA AGT CTC ATC ATT GGT GTT GTA TAG TGA CAA G-3'
SGPL1 Gly360Val_R	5'-CAA TGA TGA GAC TTT TGG GGC ATA GCC ATA CTT ATG GGT G-3'
SGPL1 Ser362Thr_F	5'-AAA GGC TCA ACA TTG GTG TTG TAT AGT GAC AAG AAG TAC-3'
SGPL1 Ser362Thr_R	5'-ACA ACA CCA ATG TTG AGC CTT TTG GGG CAT AGC CAT AC-3'
SGPL1 Tyr416Cys_F	5'-TGA GAA CGG CTG TGT TGA AGC TAC CAA ACA GAT CAT CAA AAC-3'
SGPL1 Tyr416Cys_R	5'-TAG CTT CAA CAC AGC CGT TCT CAC CGA AGT GCA TCA AGG C-3'

Silencing of ORMDL123

siRNAs targeting human *ORMDL1, 2, 3* were used to silence (knockdown) ORMDL1, 2 and 3 expressions. All siRNAs were mixed to an individual final concentration of 10 nM in reduced-serum media (Opti-MEM, 31985062, Thermo Fisher Scientific). Transfection was performed using Lipofectamine RNAiMAX transfection Reagent (13778150, Thermo Fisher Scientific) according to the manufacturer's recommendations. The media was replaced every 24 hours with fresh DMEM (10%

FBS), and cells were grown for a total of 72 hours before the start of labeling experiments. Knockdown efficiency was determined using qRT-PCR.

Isotopic labelling

For the SL labelling assay, cells were plated in 6-well plates. Cells were grown for 48 hours to 70% confluence in DMEM (10% FBS/1% P/S) (HEK293T, primary fibroblasts) or DMEM/F12 (10% FBS/1% P/S) growth media. 24 hours before harvesting, the medium was replaced with L-Serine free DMEM (C4331.0500, Genaxxon Bioscience) with 10% FBS/1% P/S and supplemented with 1mM of d_3-^{15}N-L-Serine (DNLM-6863-PK, Cambridge Isotope laboratories) with an addition of other treatments including (d7-Sa (860658), d7-So (860657) or d7-S1P (860659), Avanti Polar Lipids; FB1 (F1147), Sigma-Aldrich; Myr (M1177), Sigma-Aldrich) indicated in the figures. Cells were harvested by trypsinization, and the cell pellets washed twice with cold PBS. The pellets were frozen and stored at -20°C until extraction.

Mice tissues S1P measurement

Mice tissues were generated as described previously (30). Tissue homogenates were prepared using Precellys homogenizer. Briefly, tissues were weighed on ice and transferred to the Precellys 2mL tubes with 6 beads per tube. MeOH was added to correct the concentration of the homogenates. Then, 9 rounds of homogenization at 5500 rpm, 25 seconds each round were performed at 4°C. Tissue homogenates were used for lipid extraction and analysis, as described below.

Lipidomics analysis

Lipidomics analysis was performed as described previously (20). Briefly, extraction was performed by mixing the cell pellets, plasma, urine, or tissue homogenate with extraction buffer (60 minutes, 37°C) consisting of a mixture of methanol: methyl *tert*-butyl ether: chloroform 4:3:3 (v/v/v) and internal standards. After centrifugation (16 000 g, 10 min), the single-phase supernatant was collected, dried under N_2, and stored at -20°C. Before analysis, lipids were dissolved in MeOH and separated on a C30 LC column using gradient elution with A) Acetonitrile: Water (6:4) with 10mM ammonium acetate and 0.1% formic acid and B) Isopropanol: Acetonitrile (9:1) with 10mM ammonium acetate and 0.1% formic acid at a flow rate of 260µL/minute. Eluted lipids were analyzed on a Q-Exactive HRMS (Thermo Fisher Scientific) in positive and

negative modes using heated electrospray ionisation (HESI). MS2 fragmentation spectra were recorded in data-dependent acquisition mode. Peak integration was performed with TraceFinder 4.1 (Thermo Fisher Scientific). Lipids were identified by predicted mass (resolution 5ppm), retention time, and specific fragmentation patterns. Next, lipid concentrations were normalized to the internal standards (one per class) and total protein amount.

List of internal standards:
d5-1-deoxymethylsphinganine (SPB17:0;O, 860476, Avanti Polar Lipids) 100pmol/sample
C17 Sphingosine-1-phosphate (SPBP17:0;O2, LM2144, Avanti Polar Lipids) 50pmol/sample
1-deoxydihydroceramide (Cer18:0;O/12:0, 860460P. Avanti Polar Lipids) 100pmol/sample
1-deoxyceramide (Cer18:1;O/12:0, 860455, Avanti Polar Lipids) 100pmol/sample
Dihydroceramide (Cer18:0;O2/12:0, 860635, Avanti Polar Lipids) 100pmol/sample
Ceramide (Cer18:1;O2/12:0, 860512, Avanti Polar Lipids) 100pmol/sample
SM (SM18:1;O2/12:0, 860583, Avanti Polar Lipids) 100pmol/sample
Glucosylceramide (GlcCer18:1;O2/ /8:0, 860540, Avanti Polar Lipids) 100pmol/sample
SPLASH standard (330707, Avanti Polar Lipids) 2,5µL/sample

Transitions used for the identification of Sphingolipids:
Ceramides:
$[M+H]^+ \rightarrow [M+H - H_2O]^+$, $[M+H]^+ \rightarrow [M+H - H_2O - FA]^+$,$[M+H]^+ \rightarrow [M+H - 2xH_2O - FA]^+$
HexosylCeramides:
$[M+H]^+ \rightarrow [M+H - Hexosyl]^+$, $[M+H]^+ \rightarrow [M+H - H_2O - FA - Hexosyl]^+$, $[M+H]^+ \rightarrow [M+H - 2xH_2O - FA - Hexosyl]^+$
Sphingomyelins
$[M+H]^+ \rightarrow [PO4\text{-}Choline]^+$, $[M+H]^+ \rightarrow [M+H - H_2O - FA – PO4\text{-}Choline]^+$, $[M+H]^+ \rightarrow [M+H - 2xH_2O - FA - PO4\text{-}Choline]^+$
Sphingosine-1-phosphates
$[M+H]^+ \rightarrow [M+H - 2xH_2O - FA – PO4]^+$, $[M+H]^+ \rightarrow [M+H - H_2O - FA – PO4]^+$
Free long-chain bases (Sphingosine and Sphinganine):
$[M+H]^+ \rightarrow [M+H - H_2O]^+$, $[M+H]^+ \rightarrow [M+H – 2xH_2O]^+$

Phosphatidyl cholines

$[M+H]^+ \rightarrow [PO4\text{-}Choline]^+$, $[M+H]^+ \rightarrow [Choline]^+$

$[M+Formate]^+ \rightarrow [M+Formate - PO4\text{-}Choline - FA]^+$

Note: FA represents corresponding fatty acyl.

Protein determination

For the protein content normalization, cell pellets remaining after the lipid extraction were dissolved in urea (8M) containing 1% 2-mercaptoethanol and mixed at 800 rpm at 90°C (Thermomixer (Eppendorf)) for 20 minutes. Next, protein extracts were snap frozen using dry ice, and the whole process was repeated three times. After centrifugation (16 100 rpm, 10 minutes), supernatants were collected and used for further analysis. Total protein was determined using Bradford assay (Bio-Rad, 1:50 dilution) according to the manufacturers' recommendation.

Western blotting

Protein isolation and Western blot were performed as described elsewhere (20).

Kidneys were harvested from *Sgpl1*$^{fl/fl}$ and *Sgpl1*$^{rosa+fl/fl}$ mice after 28 days of post-tamoxifen induction. Samples were homogenized in radioimmune precipitation assay buffer (25 mM Tris-HCl (pH 7.6), 150 mM NaCl, 1% NP-40, 1% sodium deoxycholate, and 0.1% SDS) supplemented with protease inhibitors using a Tissuelyzer and then cleared by centrifugation. Primary antibodies used for immunodetection of V5-antigen were V5 Tag antibody (R960-25, Thermo Fisher Scientific, 1:2000 dilution, 1 hour at room temperature) and for Calnexin immunodetection, Anti-Calnexin (ZRB1147, Sigma-Aldrich, 1:2500 dilution, 1 hour at room temperature). As secondary antibodies horseradish peroxidase–conjugated anti-mouse (NC2294470, Thermo Fisher Scientific; 1:10 000, 1 hour at room temperature) and anti-rabbit (12-348, Thermo Fisher Scientific; 1:10 000, 1 hour at room temperature) IgGs were used.

These antibodies were used to detect the protein level: anti-mouse SPL (SAB2109200, MilliporeSigma), rabbit anti-GAPDH (sc-25778, Santa Cruz Biotechnology and HRP-conjugated secondary antibodies 111-035-144, Goat Anti-Rabbit IgG (H + L), Jackson Immuno Research; sc-2020.

Toxicity assays

For the toxicity assay cells were grown for 72 hours in the 96-well plates with treatment (So (860490), Avanti Polar Lipids; FB1 (F1147), Sigma-Aldrich; Genz (5.38285), Sigma-Aldrich), as indicated in the figures. Next CellTiter-Glo ® Luminescent Cell Viability Assay (G7570, Promega) was performed according to the manufacturer's recommendations. Chemiluminesce signal was detected using TECAN infinite M 200 Pro reader. All conditions were corrected for the solvent concentration.

Live cell microscopy

For the live cell microscopy, cells were grown in 96-well plates in the incubator at 5% CO_2 and 37°C. Indicated treatment (JTE 013 (J4080), Fasudil (CDS021620), FTY720 (SML0700), Sigma-Aldrich) was added by media exchange. Then, the plate was immediately transferred to a live-cell imaging microscope (Olympus IX81) with a motorized stage, fitted with an incubator with pre-heated humidified atmosphere (Ibidi mixer), and kept at 37°C and 5% CO_2. Phase-contrast images were acquired at 20x magnification every 15 minutes for 48 hours. Four images per well were acquired and compiled. Percentage contracted cells was acquired by selecting four 10mm rectangles (regions of interest) per well and then contracted cells and non-contracted cells were counted manually using ImageJ software. The same positions of the rectangles per well were used at all timepoints and conditions. Percentage of contracted cells per well was calculated as average of four percentages in rectangles. All original images of cut rectangles used for manual counting are available.

Scratch assay

Scratch assay was performed as described previously (31). Briefly, fibroblasts were seeded in 12-well plates for 48 hours. Next, cell proliferation was stopped by 2-hour incubation with Mitomycin C (M4287, Sigma-Aldrich, 10 µg/ml). Then, a scratch was introduced in the middle of the well with a 20 µL pipette tip. To remove cell debris, the wells were rinsed once with PBS, and fresh DMEM (10% FBS/1 % P/S) supplemented with the specified treatments was added. Plates were transferred to a live-cell imaging microscope (Olympus IX81) equipped with a motorized stage and fitted with an incubator featuring a pre-heated, humidified atmosphere (Ibidi mixer, Ibidi GmbH), which was maintained at 37°C and 5% CO_2. Phase-contrast pictures were acquired at 10x magnification every 30 minutes for 48 hours.

Fluorescence microscopy

For fluorescence microscopy, cells were grown in 96-well plates in an incubator at 5% CO_2 at 37°C. Indicated treatments were added by exchange of the media. After the given time (indicated in the figures), cells were washed 3 times with PBS and fixed using 4% PFA for 30 minutes. Next, cells were washed 3 times with PBS and then incubated for 1 hour with DAPI (D9542 , Sigma-Aldrich, 1 µM in PBS) and Phalloidin-665 (18846, Sigma-Aldrich, 0.5 µM in PBS). Further, cells were washed with PBS and imaged immediately. Images were acquired using a fluorescence microscope (Olympus IX81) with a motorized stage at 20x magnification.

For the phalloidin staining, kidney sections were deparaffinized and rehydrated. A gentle heat-retrieval was performed in citrate buffer pH 6.0 (10 mM, 95–98 °C, ~10 min), then cooled in PBS. WT1 (Wilms tumor protein, sc-7385), a marker for glomeruli, and Alexa Fluor 568 phalloidin (ThermoFischer Scientific, A12380) in normal horse serum were applied and incubated for 30 minutes at room temperature in the dark. Hoechst in VectaShield (Vector Laboratories) was used to mount the slides. Images were captured by a Zeiss LSM 710 confocal microscope.

Animals

Sgpl1 Knockout mice in which the *Sgpl1* gene is constitutively disrupted (*Sgpl1*$^{-/-}$ mice) have been described previously (32). Heterozygous (HET) knockout breeders were mated, and newborns were genotyped by toe biopsy. Transgenic mice harboring *Sgpl1*$^{fl/fl}$ and *Sgpl1*$^{rosa\ (cre/ERT2)+fl/fl}$ allele were gifted from UCSD collaborator and described previously (32).

Studies

Animal experiments were approved by the IRB UCSF (San Francisco). The Patient sample was collected for diagnostic purposes. All subjects involved provided written informed consent.

Serum albumin, creatinine, and blood urea nitrogen (BUN)

Serum albumin, creatinine, and BUN were measured using the COBAS INTEGRA 400 plus instrument (Roche Diagnostics) by the University of California Davis Comparative Pathology Laboratory (Davis, California, USA).

Determination of albumin to creatine ratio (ACR)

The albumin to creatinine ratio in urine from *Sgpl1*$^{fl/fl}$, *Sgpl1*$^{rosa+fl/fl}$ and *Sgpl1*$^{rosa+fl/fl}$+Fasudil was determined using the Ethos/Exocell's immunospecific Albumin ELISA and creatinine companion kit according to manufactured protocol.

Periodic acid-Schiff staining (PAS)

PAS staining was performed on 5 micron kidney sections from *Sgpl1*$^{fl/fl}$, *Sgpl1*$^{rosa+fl/fl}$ *Sgpl1*$^{rosa+fl/fl}$+Fasudil, *Sgpl1*$^{-/-}$ and WT mice as we described previously (33).

The percent glomerulosclerosis was determined by visual inspection. A total of 50 glomeruli and surrounding tissues were evaluated to quantify abnormalities including segmentally sclerosed glomeruli, glomeruli displaying mesangial hypercellularity, and interstitial fibrosis. Both kidneys of N=3 mice per group were analysed.

Casts were scored as either not present or 1, 2, 3 or 4+ in severity, with 1+ indicating rare casts and 4+ indicating 80% or more tubules filled with PAS-positive material.

Image analysis

Image analysis was performed using CellProfiler 4.2.1 using an in-house made pipeline. First, the Nucleus area was segmented as a primary object (Otsu thresholding method) using the DAPI channel image. Second, cellular area was identified and segmented as a secondary object from Nuclear area in Phalloidin channel image (Propagation method using Minimum Cross-Entropy thresholding). Then, log10(Cellular area/Nucleus area) was calculated per object and the average per well was used for further quantification.

Data analysis, statistics and figures

Data analysis and figure preparations were done using GraphPad Prism 9.5.1 (for Bar graphs and stack plots) and Excel. Statistical analysis was performed in GraphPad Prism 9.5.1. The individual statistical methods used are indicated in the figures. A p-value of <0.05 was considered significant.

Illustrations were made using BioRender (BioRender.com). Final figures were prepared using Affinity Designer 2.

Data availability

Data are available in the supplemental file: "SPLIS Source data.xlsx" and from the corresponding author on request

Author contributions:

AM performed main experiments and analysis, interpreted the data and wrote the manuscript. RK and JDS. performed mouse experiments, analyzed samples and reviewed the manuscript. KB identified the patient, collected patient specimens and identified the mutation. FB analyzed impact of SPLIS Mutations on SPL structure. TH supervised the study, edited and critically revised the manuscript.

Funding Support:

This work is the result of NIH funding, in whole or in part, and is subject to the NIH Public Access Policy. Through acceptance of this federal funding, the NIH has been given a right to make the work publicly available in PubMed Central.

RK was supported by NIH U2C/TL1 LAUNCH program (National Institute of Diabetes and Digestive and Kidney Diseases [NIDDK] grant 5TL1DK139565-03. JS received support from National Institutes of Health (NIH)/Office of the Director R21OD037868-01, NIH/NICHD R01HD113778, California Institute of Regenerative Medicine (CIRM) DISC2-13072, and grants from the RTW Charitable Foundation and Harrington Discovery Institute. TH was supported by the Swiss National Science Foundation (SNF 310030_215134) and by the SNF under the frame of the European Joint Program on Rare Diseases (EJP RD+SNF 32ER30_187505).

References

1. Lovric S, Goncalves S, Gee HY, Oskouian B, Srinivas H, Choi WI, et al. Mutations in sphingosine-1-phosphate lyase cause nephrosis with ichthyosis and adrenal insufficiency. *Journal of Clinical Investigation.* 2017;127(3):912-28.
2. Pulli I, Asghar MY, Kemppainen K, and Tornquist K. Sphingolipid-mediated calcium signaling and its pathological effects. *Biochim Biophys Acta Mol Cell Res.* 2018;1865(11 Pt B):1668-77.
3. Duan M, Gao P, Chen SX, Novak P, Yin K, and Zhu X. Sphingosine-1-phosphate in mitochondrial function and metabolic diseases. *Obes Rev.* 2022;23(6):e13426.
4. Hannun YA, and Obeid LM. Sphingolipids and their metabolism in physiology and disease. *Nat Rev Mol Cell Biol.* 2018;19(3):175-91.
5. Saba JD. Fifty years of lyase and a moment of truth: sphingosine phosphate lyase from discovery to disease[S]. *Journal of Lipid Research.* 2019;60(3):456-63.
6. Keller N, Midgley J, Khalid E, Lesmana H, Mathew G, Mincham C, et al. Factors influencing survival in sphingosine phosphate lyase insufficiency syndrome: a retrospective cross-sectional natural history study of 76 patients. *Orphanet J Rare Dis.* 2024;19(1):355.
7. Pournasiri Z, Madani A, Nazarpack F, Sayer JA, Chavoshzadeh Z, Nili F, et al. Sphingosine phosphate lyase insufficiency syndrome: a systematic review. *World J Pediatr.* 2023;19(5):425-37.
8. Tran P, Jamee M, Pournasiri Z, Chavoshzadeh Z, and Sullivan KE. SGPL1 Deficiency: Nephrotic Syndrome with Lymphopenia. *J Clin Immunol.* 2023;43(1):72-5.
9. Bektas M, Allende ML, Lee BG, Chen W, Amar MJ, Remaley AT, et al. Sphingosine 1-phosphate lyase deficiency disrupts lipid homeostasis in liver. *J Biol Chem.* 2010;285(14):10880-9.
10. Saba JD, Keller N, Wang JY, Tang F, Slavin A, and Shen YZ. Genotype/Phenotype Interactions and First Steps Toward Targeted Therapy for Sphingosine Phosphate Lyase Insufficiency Syndrome. *Cell Biochem Biophys.* 2021;79(3):547-59.
11. Smith CJ, Williams JL, Hall C, Casas J, Caley MP, O'Toole EA, et al. Ichthyosis linked to sphingosine 1-phosphate lyase insufficiency is due to aberrant sphingolipid and calcium regulation. *Journal of Lipid Research.* 2023;64(4).
12. Gault CR, Obeid LM, and Hannun YA. An overview of sphingolipid metabolism: from synthesis to breakdown. *Adv Exp Med Biol.* 2010;688:1-23.
13. Kono M, Hoachlander-Hobby LE, Majumder S, Schwartz R, Byrnes C, Zhu HL, and Proia RL. Identification of two lipid phosphatases that regulate sphingosine-1-phosphate cellular uptake and recycling. *Journal of Lipid Research.* 2022;63(6).
14. Goto H, Miyamoto M, and Kihara A. Direct uptake of sphingosine-1-phosphate independent of phospholipid phosphatases. *Journal of Biological Chemistry.* 2021;296.
15. Xie T, Liu P, Wu X, Dong F, Zhang Z, Yue J, et al. Ceramide sensing by human SPT-ORMDL complex for establishing sphingolipid homeostasis. *Nat Commun.* 2023;14(1):3475.
16. Kihara A. Sphingosine 1-phosphate is a key metabolite linking sphingolipids to glycerophospholipids. *Bba-Mol Cell Biol L.* 2014;1841(5):766-72.
17. Gandy KAO, Canals D, Adada M, Wada M, Roddy P, Snider AJ, et al. Sphingosine 1-phosphate induces filopodia formation through S1PR2 activation of ERM proteins. *Biochem J.* 2013;449:661-72.
18. Zhao P, Liu ID, Hodgin JB, Benke PI, Selva J, Torta F, et al. Responsiveness of sphingosine phosphate lyase insufficiency syndrome to vitamin B6 cofactor supplementation. *J Inherit Metab Dis.* 2020;43(5):1131-42.
19. Winkler MS, Nierhaus A, Holzmann M, Mudersbach E, Bauer A, Robbe L, et al. Decreased serum concentrations of sphingosine-1-phosphate in sepsis. *Crit Care.* 2015;19:372.
20. Lone MA, Aaltonen MJ, Zidell A, Pedro HF, Morales Saute JA, Mathew S, et al. SPTLC1 variants associated with ALS produce distinct sphingolipid signatures through impaired interaction with ORMDL proteins. *J Clin Invest.* 2022;132(18).
21. Xie T, Liu P, Wu XY, Dong FT, Zhang ZK, Yue J, et al. Ceramide sensing by human SPT-ORMDL complex for establishing sphingolipid homeostasis. *Nature Communications.* 2023;14(1).
22. Hagen-Euteneuer N, Lutjohann D, Park H, Merrill AH, and van Echten-Deckert G. Sphingosine 1-Phosphate (S1P) Lyase Deficiency Increases Sphingolipid Formation via Recycling at the Expense of de Novo Biosynthesis in Neurons. *Journal of Biological Chemistry.* 2012;287(12):9128-36.

23. Herr DR, Fyrst H, Phan V, Heinecke K, Georges R, Harris GL, and Saba JD. Sply regulation of sphingolipid signaling molecules is essential for Drosophila development. *Development.* 2003;130(11):2443-53.
24. Mitroi DN, Karunakaran I, Graler M, Saba JD, Ehninger D, Ledesma MD, and van Echten-Deckert G. SGPL1 (sphingosine phosphate lyase 1) modulates neuronal autophagy via phosphatidylethanolamine production. *Autophagy.* 2017;13(5):885-99.
25. Spiegel S, and Milstien S. Sphingosine-1-phosphate: an enigmatic signalling lipid. *Nat Rev Mol Cell Biol.* 2003;4(5):397-407.
26. Zhang J, Chen S, Xiang H, Xiao J, Zhao S, Shu Z, et al. S1PR2/Wnt3a/RhoA/ROCK1/beta-catenin signaling pathway promotes diabetic nephropathy by inducting endothelial mesenchymal transition and impairing endothelial barrier function. *Life Sci.* 2023;328:121853.
27. Volzke A, Koch A, Meyer Zu Heringdorf D, Huwiler A, and Pfeilschifter J. Sphingosine 1-phosphate (S1P) induces COX-2 expression and PGE2 formation via S1P receptor 2 in renal mesangial cells. *Biochim Biophys Acta.* 2014;1841(1):11-21.
28. Haberkant P, Stein F, Hoglinger D, Gerl MJ, Brugger B, van Veldhoven PP, et al. Bifunctional Sphingosine for Cell-Based Analysis of Protein-Sphingolipid Interactions. *Acs Chem Biol.* 2016;11(1):222-30.
29. Engel R. 2022.
30. Zhao PM, Tassew GB, Lee JY, Oskouian B, Munoz DP, Hodgin JB, et al. Efficacy of AAV9-mediated SGPL1 gene transfer in a mouse model of S1P lyase insufficiency syndrome. *Jci Insight.* 2021;6(8).
31. Karsai G, Steiner R, Kaech A, Lone MA, von Eckardstein A, and Hornemann T. Metabolism of HSAN1- and T2DM-associated 1-deoxy-sphingolipids inhibits the migration of fibroblasts. *J Lipid Res.* 2021;62:100122.
32. Kaur P, Karuppuchamy T, Chilukuri A, Kim M, Urrete J, Shen Z, et al. S1P Lyase Inhibition Increased Intestinal S1P, Disrupted the Intestinal Barrier and Aggravated DSS-Induced Colitis. *Inflamm Bowel Dis.* 2025;31(7):1994-2006.
33. Khan R, Oskouian B, Lee JY, Hodgin JB, Yang Y, Tassew G, and Saba JD. AAV-SPL 2.0, a Modified Adeno-Associated Virus Gene Therapy Agent for the Treatment of Sphingosine Phosphate Lyase Insufficiency Syndrome. *Int J Mol Sci.* 2023;24(21).
34. Abramson J, Adler J, Dunger J, Evans R, Green T, Pritzel A, et al. Accurate structure prediction of biomolecular interactions with AlphaFold 3. *Nature.* 2024;630(8016):493-500.

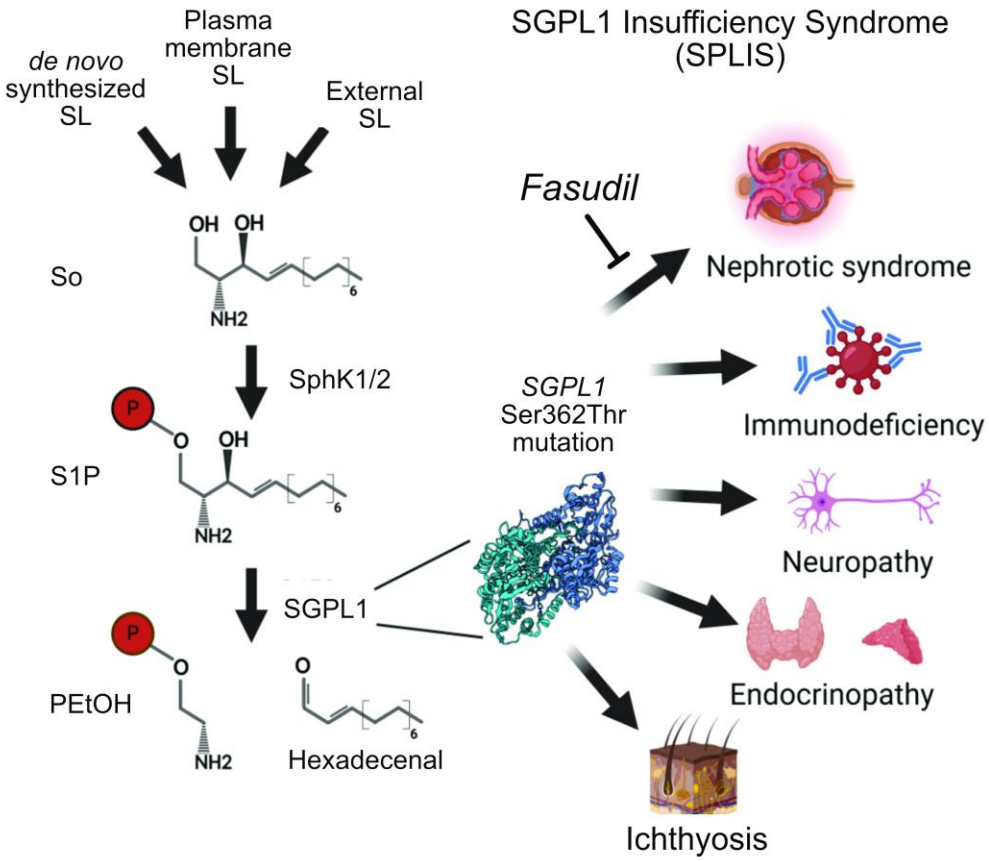

Graphical abstract

Created in BioRender. Hornemann, T. (2026) https://BioRender.com/0wt5qdn

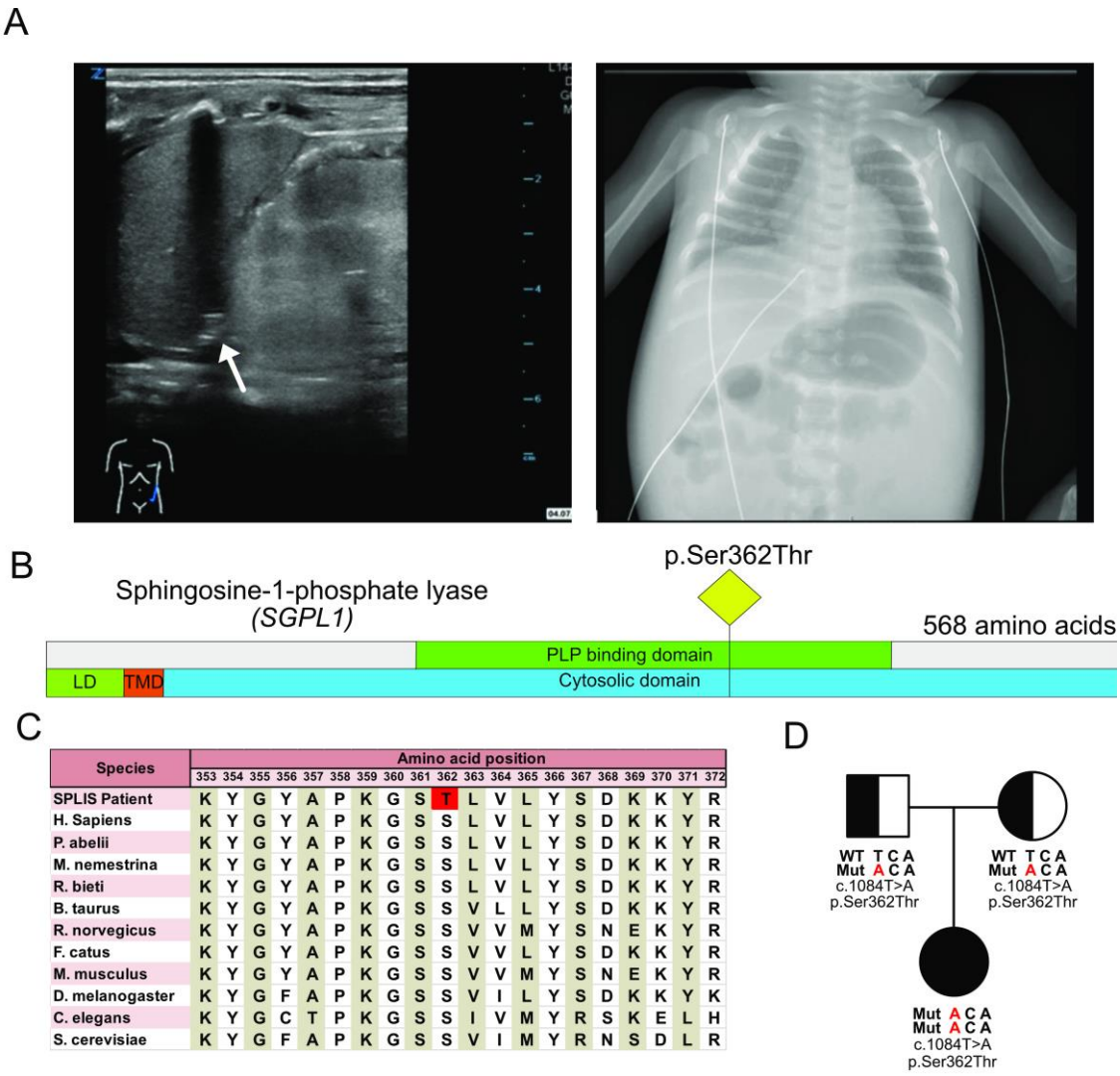

Figure 1: **Clinical and molecular characterization of the new SPLIS-causing *SGPL1* mutation p.Ser362Thr**. **(A)** Sonographic and X-ray imaging of a patient with the *SGPL1* mutation (p.Ser362Thr). Left: Sonographic image showing a hyperechogenic kidney and adrenal calcifications (arrow). Only the left kidney and adrenal gland are depicted. Right: X-ray image revealing adrenal calcifications. **(B)** Schematic representation of the human *SGPL1* gene with an up-to-scale domain architecture. The SPLIS-associated mutation is marked with a yellow rectangle. **(C)** Conservation analysis of amino acid residues surrounding the SPLIS-

causing mutation in *SGPL1*. The patient mutation (p.Ser362Thr) is highlighted in red. **(D)** Pedigree of the affected family, illustrating the segregation of the *SGPL1* variant (*NM_003901.3* c.1084T>A, p.Ser362Thr, Chr10(hg19):g.72633132T>A). **(E)** SL profile of primary skin fibroblasts from the SPLIS patient versus healthy controls (N=3). Bar plots represent the mean ± SD of sums for each SL class. Statistical significance was assessed using a t-test, with multiple testing correction applied via the two-stage step-up method (Benjamini, Krieger, and Yekutieli). n.s. = non-significant; * = q < 0.05; ** = q < 0.005; *** = q < 0.0005.

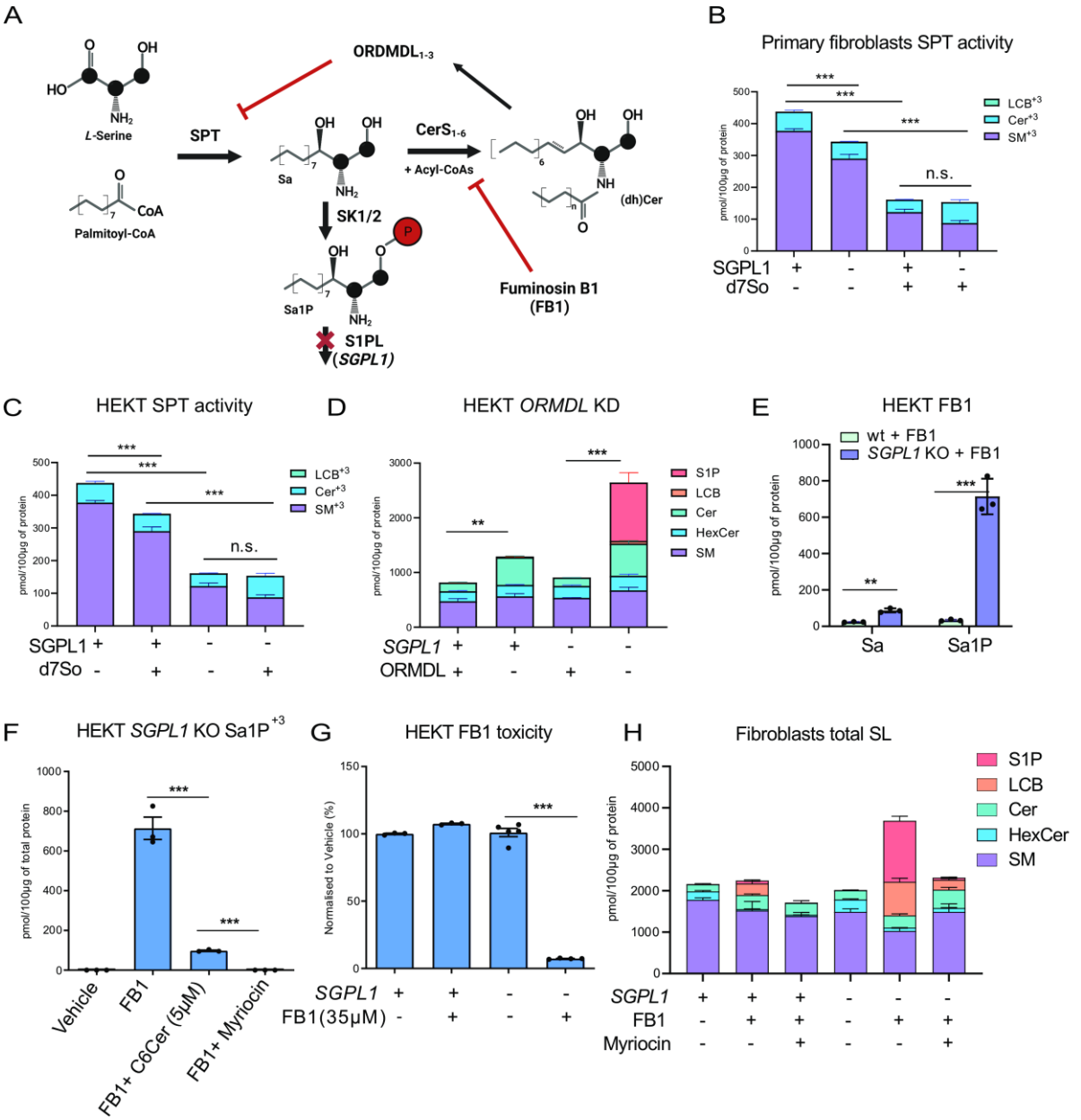

Figure 2: SPT regulation via the ORMDL–ceramide axis prevents toxic S1P accumulation in SGPL1-deficient cells.

(A) Schematic overview of de novo sphingolipid (SL) synthesis and its regulation by serine palmitoyltransferase (SPT). **(B)** Reduced SPT activity in SPLIS primary skin fibroblasts lacking SGPL1 (SGPL1–) compared with control fibroblasts (SGPL1+). Cells were supplemented with exogenous sphingolipids (+) or vehicle (–) to assess homeostatic regulation. (C) SPT activity in HEK293T SGPL1 knockout (KO) cells compared with WT cells, with or without d7-sphingosine (d7-So) supplementation. **(D)** Total SL levels after ORMDL1–3 knockdown in

HEK293T SGPL1 KO and WT cells. Cells were transfected with scrambled (ORMDL+) or ORMDL-targeting siRNAs (ORMDL–) using Lipofectamine 3000 for 72 h before analysis**. (E)** Total sphinganine (Sa) and sphinganine-1-phosphate (Sa-1-P) levels in HEK293T SGPL1 KO and WT cells treated with the ceramide synthase inhibitor fumonisin B1 (FB1). **(F)** De novo formation of Sa-1-P in SGPL1 KO cells treated with vehicle, FB1, FB1 plus cell-permeable C6-ceramide (C6Cer), or FB1 plus the SPT inhibitor myriocin. **(G)** FB1 toxicity assay in HEK293T SGPL1 KO and WT cells. Cells were treated with FB1 for 72 h and ATP levels were quantified using the CellTiter-Glo assay**. (H)** Total SL levels in SPLIS fibroblasts (SGPL1–) and control fibroblasts (SGPL1+) treated with vehicle (MeOH), FB1 or FB1+myriocin.
SPT activity was determined by measuring incorporation of d3-15N-serine after 24 h. Plots represent mean ± SD (N = 3). Hexosylceramides (HexCer) represent the sum of glucosylceramide and galactosylceramide. SL levels were quantified by LC-MS/MS after lipid extraction. Statistical significance was assessed using Student's t-test with multiple-testing correction using the two-stage step-up method of Benjamini, Krieger, and Yekutieli. * $p < 0.05$; ** $p < 0.01$; *** $p < 0.001$. Toxicity assay data were normalized to the mean of vehicle-treated cells (N = 4). *Created in BioRender. Hornemann, T. (2026) https:// BioRender.com/0wt5qdn*

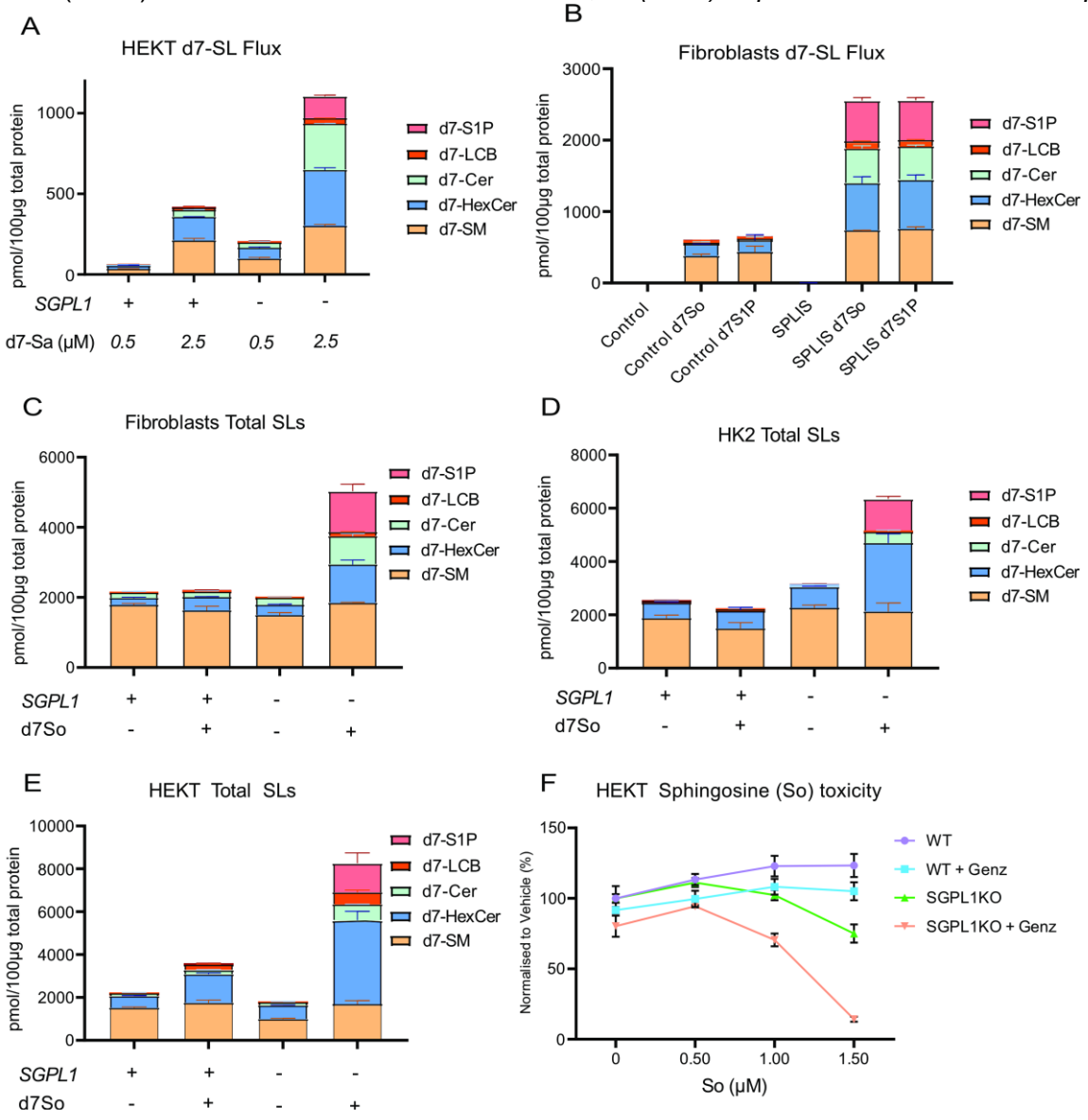

Figure 3: **Synthesis of higher-order sphingolipids (SL) acts as an "escape" mechanism to prevent toxic S1P accumulation in SPLIS. (A)** d7-SL profiles following supplementation

with d7-sphinganine (d7-Sa, 0.5 µM or 2.5 µM) in *HEK293T SGPL1* KO and WT cells. **(B)** d7-SL levels in primary SPLIS fibroblasts and control fibroblasts after treatment with vehicle, d7-sphingosine (d7-So, 0.5 µM), or d7-sphingosine-1-phosphate (d7-S1P, 0.5 µM) for 24 hours. **(C–E)** Total SL levels in three different *SGPL1*-deficient cell lines—primary fibroblasts (**C**), HK2 cells (**D**), and *HEK293T* cells (**E**)—compared to corresponding controls after 24-hour supplementation with vehicle (MeOH) or d7-So (2.0 µM). Total SL levels were calculated as the sum of d7-labeled and unlabeled SL species. Bar and stacked plots represent mean ± SD (N=3) for the indicated SL classes. Galactosylceramides and glucosylceramides are cumulatively represented as hexosylceramides (HexCer). SL levels were quantified via LC-MS/MS following lipid extraction. **(F)** ATP-based sphingosine (So) toxicity assay in *HEK293T SGPL1* KO and WT cells. Glucosylceramide synthesis was inhibited using the glucosylceramide synthase (GCS) inhibitor Genz-123346 (Genz). Cells were exposed to increasing concentrations of So for 72 hours, and total ATP levels were quantified using the CellTiter-Glo assay. Data from the toxicity assay were normalized to the average of vehicle-treated cells (N=4).

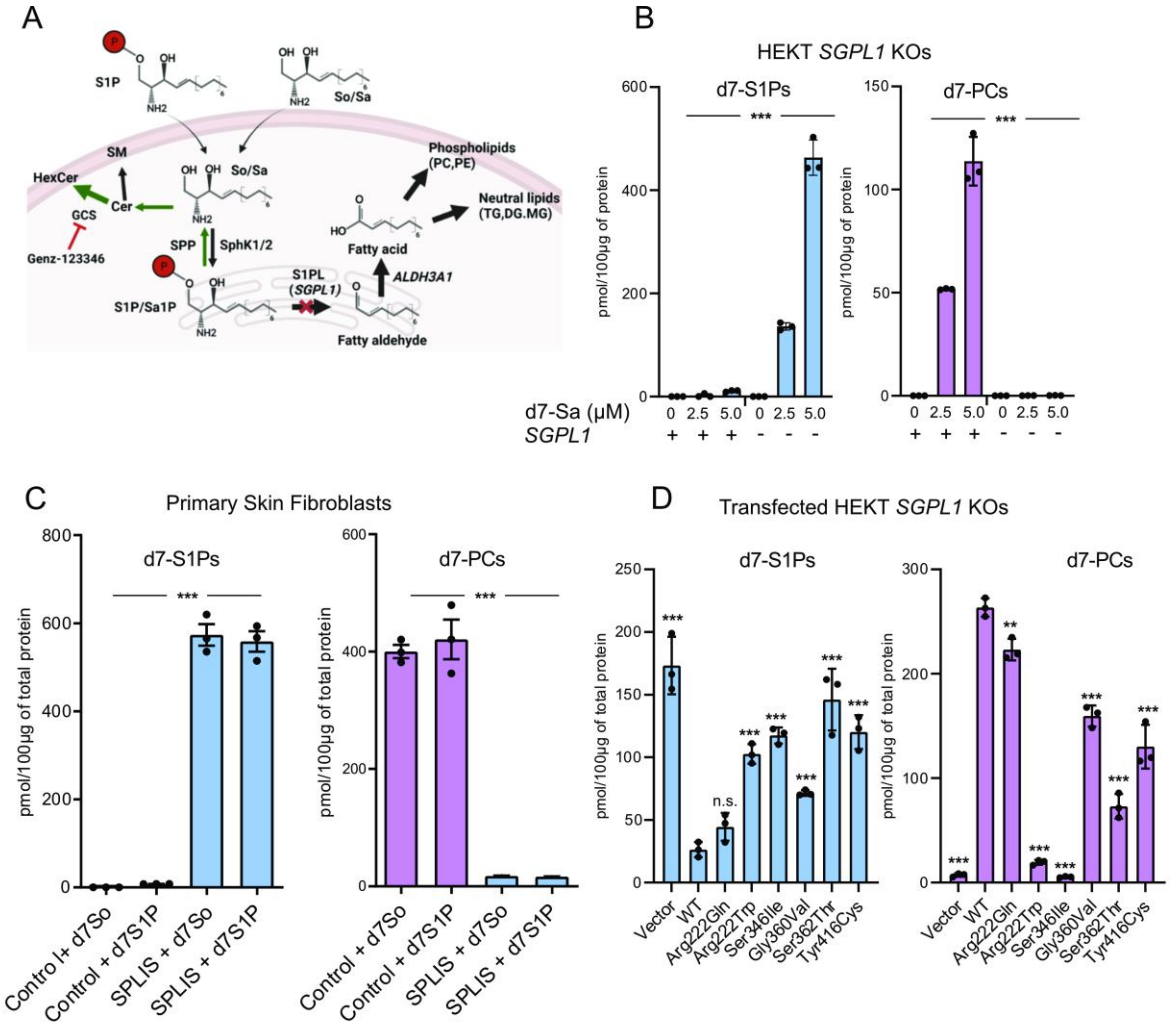

Figure 4: Analysis of sphingolipid metabolism and the impact of *SGPL1* mutations. **(A)** Schematic representation of the metabolism of externally supplemented sphingolipids (SL). **(B)** Levels of d7-S1P and d7-PC after 24 hours of incubation with increasing concentrations of d7-sphinganine (d7-Sa) in *HEK293T SGPL1* KO (*SGPL1* -) and WT (*SGPL1* +) cells. Increasing d7-Sa concentrations correlate with higher d7-PC levels in WT cells, a capability diminished in *SGPL1* KO cells, which instead show an accumulation of d7-S1P. **(C)**

Levels of d7-S1P and d7-PC after 24 hours of incubation with vehicle, d7-sphingosine (d7-So, 0.5 µM), or d7-S1P (0.5 µM) in SPLIS fibroblasts compared to control fibroblasts. **(D)** Levels of d7-S1P and d7-PC after 24 hours of incubation with d7-Sa (2.0 µM) in *HEK293T SGPL1* KO cells expressing WT *SGPL1*, an empty vector (EV), or six SPLIS-associated *SGPL1* variants. Bar plots represent mean ± SD (N=3). d7-S1P and d7-PC levels were analyzed using LC-MS/MS following lipid extraction. Statistical significance was analyzed by one-way ANOVA followed by Dunnett's multiple-comparison test comparing each mutant to WT. n.s.= not significant, ** = p < 0.005; *** = p < 0.0005. *Created in BioRender. Hornemann, T. (2026) https://BioRender.com/0wt5qdn*

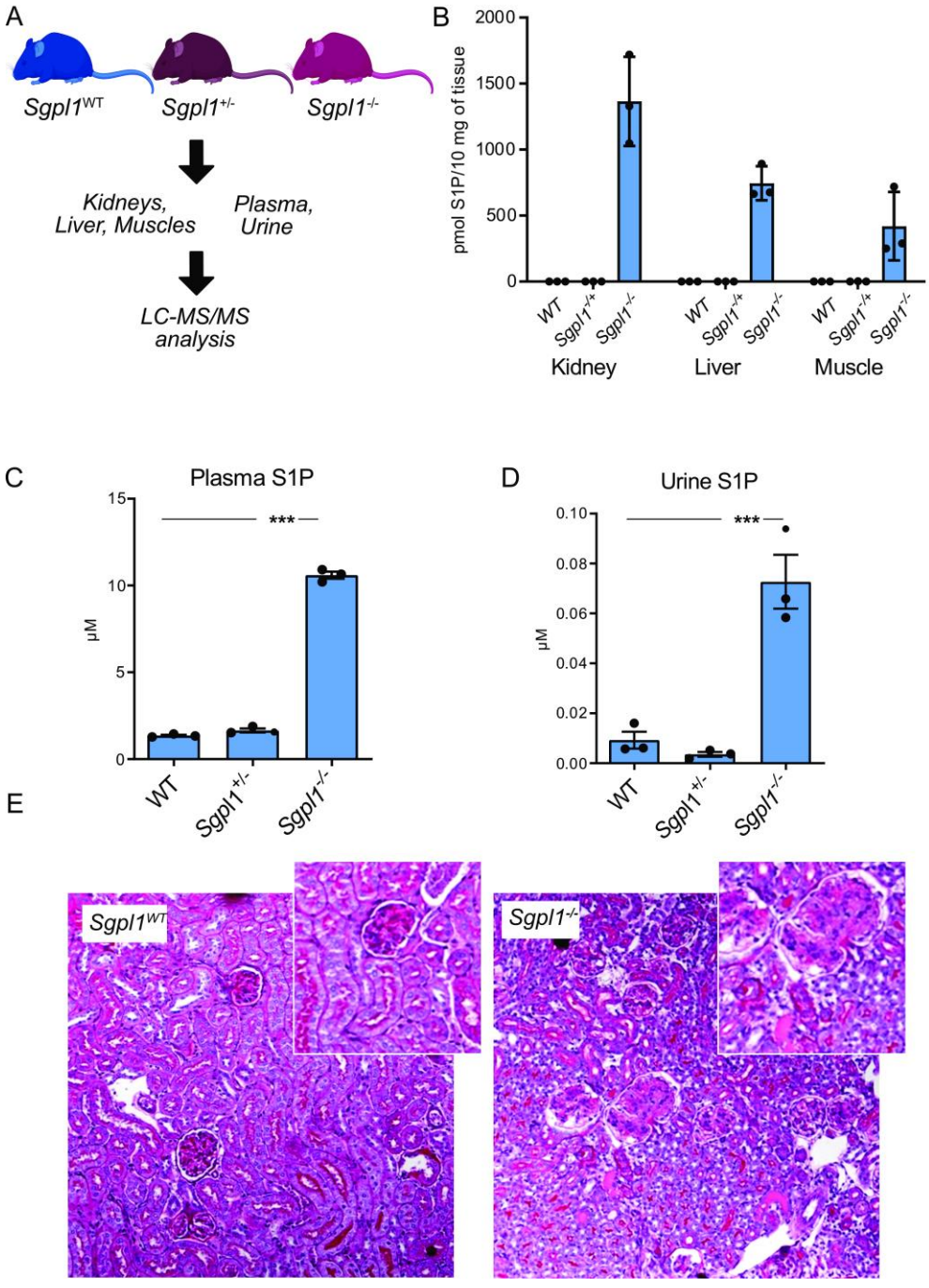

Figure 5: Analysis of S1P levels and kidney pathology in *Sgpl1* mice. **(A)** Schematic representation of tissue and body fluid sample collection from *Sgpl1* WT,

Sgpl1$^{+/-}$, and *Sgpl1*$^{-/-}$ mice. **(B)** Total S1P levels in tissues from *Sgpl1* WT (N=3), *Sgpl1*$^{+/-}$ (N=3), and *Sgpl1*$^{-/-}$ (N=3) mice. **(C)** Total plasma S1P levels in *Sgpl1* WT (N=3), *Sgpl1*$^{+/-}$ (N=3), and *Sgpl1*$^{-/-}$ (N=3) mice. **(D)** Total urinary S1P levels in *Sgpl1* WT (N=3), *Sgpl1*$^{+/-}$ (N=3), and *Sgpl1*$^{-/-}$ (N=3) mice. Bar plots represent mean ± SD (N=3). S1P levels were measured using LC-MS/MS. Statistical significance was calculated using a two-tailed *t*-test. Differences between WT and *Sgpl1*$^{-/-}$ were highly significant ($p < 0.0001$). **(E)** Kidney cortex histology of wild-type (WT) and *SGPL1* knockout (KO) mice stained with periodic acid-Schiff (PAS) stain. (Left, with inset detail): WT kidney cortex shows uniform glomeruli with normal size and cellularity. (Right, with inset detail): *SGPL1* KO kidney cortex displays protein casts and glomeruli with heterogeneity in size and appearance, mesangial expansion, hypercellularity, and collagen deposition. Percent glomerulosclerosis: WT = 0%; KO = 37%; 50 or more glomeruli were analyzed per genotype. Scale bar = 100 µm. *Created in BioRender. Hornemann, T. (2026) https://BioRender.com/0wt5qdn*

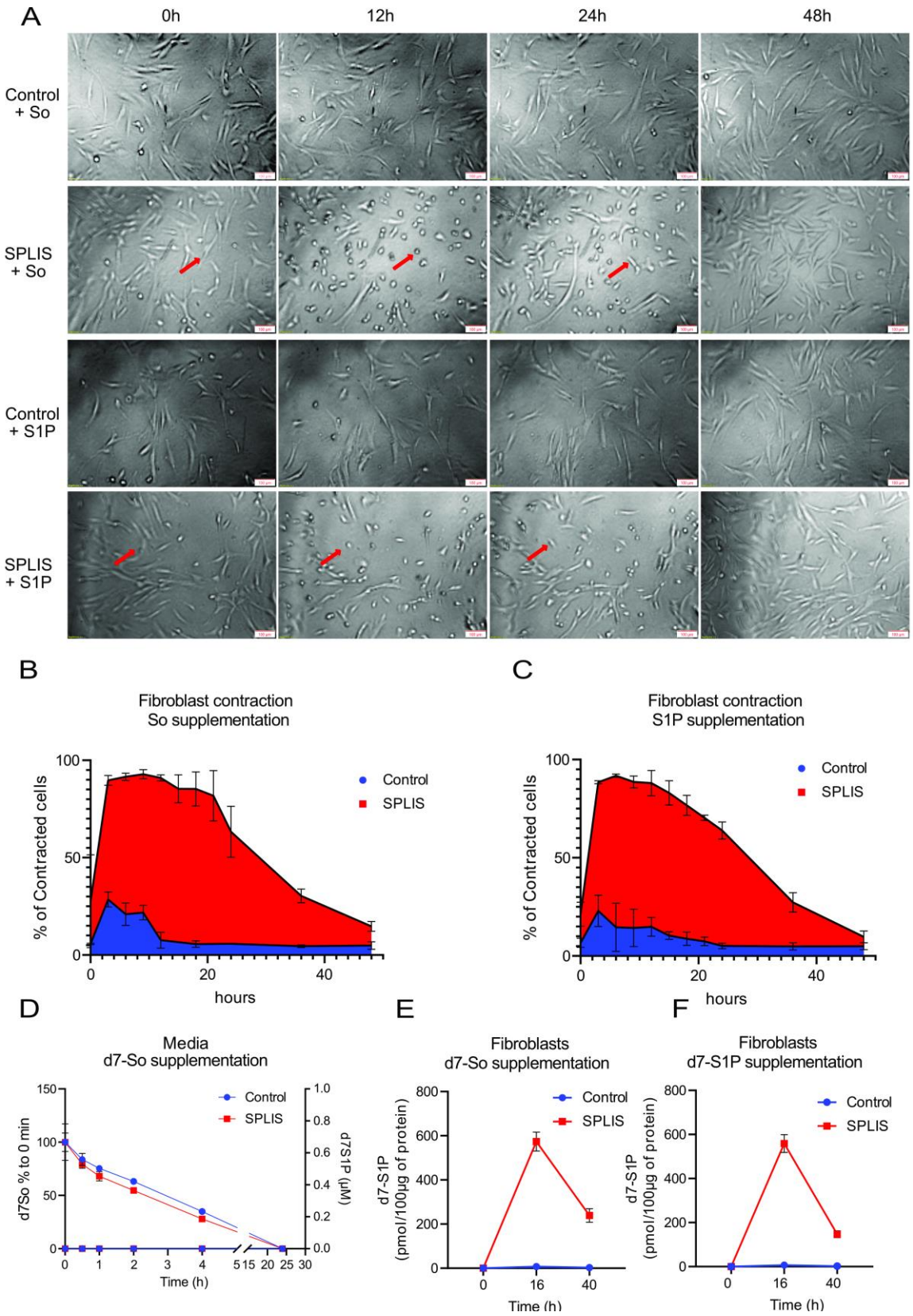

Figure 6: Cytoskeletal dynamics and lipid metabolism in SPLIS fibroblasts after So or S1P supplementation. **(A)** Live-cell imaging of SPLIS fibroblasts showing cell contraction after So or S1P supplementation. Red arrows indicate contracted cells. Scale bars: 100 µm. **(B, C)** Quantification of the percentage of contracted cells per well after So or S1P supplementation in SPLIS fibroblasts and control fibroblasts.

(D) Time-dependent uptake of d7-So (left axis) and release of d7-S1P (right axis) into the medium in cultured SPLIS and control fibroblasts. Data were normalized to the 0-hour time point. d7-So was fully absorbed within 24 hours, with no parallel release of d7-S1P into the medium. **(E)** Timeline of intracellular d7-S1P levels following supplementation with d7-So (0.5 µM) in SPLIS and control fibroblasts. **(F)** Timeline of cellular d7-S1P levels after supplementation with d7-S1P (0.5 µM) in SPLIS and control fibroblasts. Data points are represented as mean ± SD (N=3). Sphingolipid (SL) levels were analyzed using LC-MS/MS following lipid extraction.

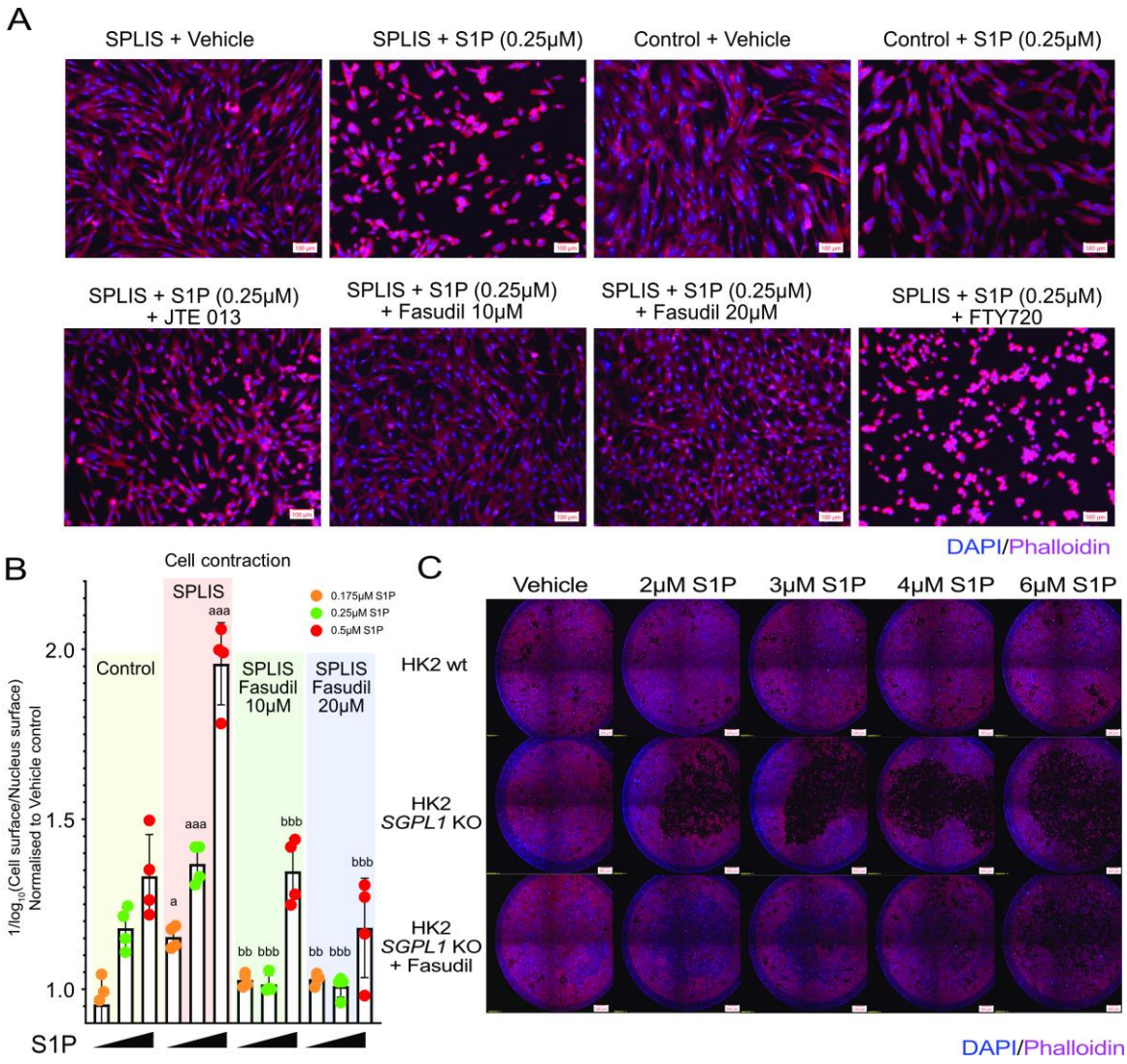

Figure 7: Fasudil rescues S1P induced cytoskeletal phenotypes in SPLIS fibroblasts and *SGPL1*-deficient HK2 cell line. (A) Fluorescence imaging of SPLIS primary fibroblasts and control fibroblasts treated with vehicle (MeOH) or S1P (0.25 µM) for 6 hours. Cells were also treated with the ROCK inhibitor (Fasudil), the sphingosine-1-phosphate receptor 2 inhibitor (JTE013), or the sphingosine-1-phosphate receptor 1 modulator (Fingolimod, FTY720). After treatment, cells were fixed with 4% PFA and stained with Phalloidin (actin) and DAPI (nucleus). Scale bars: 100 µm. **(B)** Quantification of cell contraction. Compiled images of whole wells were analyzed using CellProfiler software. Cell contraction was defined by the formula 1/log10(Cell surface/Nucleus surface). Values were normalized to the average of vehicle-treated cells. Data are represented as mean ± SD (N=4). Statistical analysis was performed using a two-tailed parametric t-test. a: Comparison between control and SPLIS fibroblasts at the same S1P concentration (a = $p < 0.05$, aa = $p < 0.005$, aaa = $p < 0.0005$). b: Comparison between SPLIS fibroblasts treated without or with two concentrations of Fasudil

(ROCK inhibitor) (b = p < 0.05, bb = p < 0.005, bbb = p < 0.0005). **(C)** Impairment of renal epithelium formation in *SGPL1* KO human proximal tubule cells (HK2) after S1P supplementation. *SGPL1* KO or WT HK2 cells were grown for 72 hours in the presence of increasing S1P concentrations, with or without Fasudil, as indicated. Cells were fixed with 4% PFA and stained with Phalloidin (actin) and DAPI (nucleus). Whole wells were imaged using fluorescence microscopy. Representative images from three independent replicates are shown. Scale bars: 500 µm.

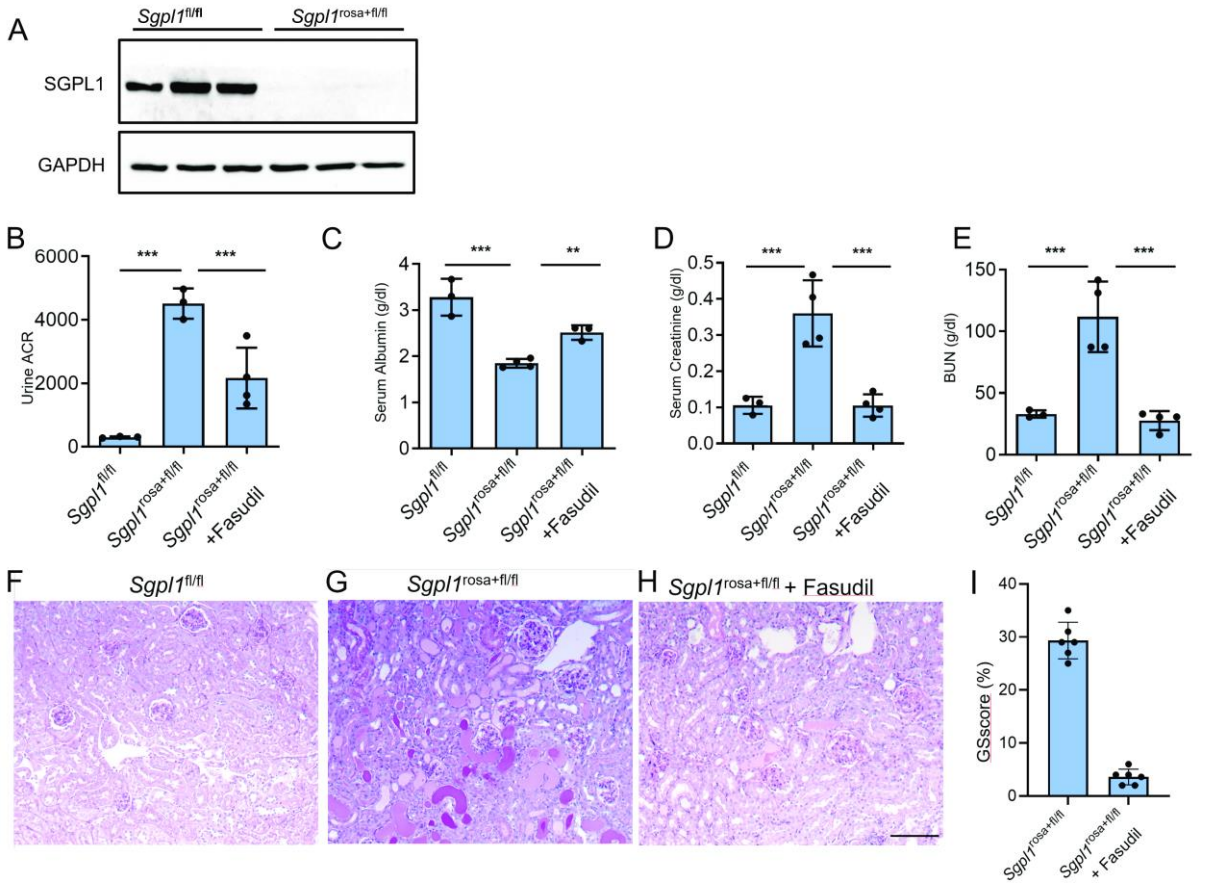

Figure 8: Effect of Fasudil treatment in *Sgpl1*$^{rosa+fl/f}$ mice. (A) Immunoblotting from the kidneys of *Sgpl1*$^{fl/fl}$ and *Sgpl1*$^{rosa+fl/fl}$ mice confirms the successful disruption of SPL in *Sgpl1*$^{rosa+fl/fl}$ mice after tamoxifen induction. **(B-E)** Urine ACR (ug of Albumin/ mg of creatinine), Serum albumin, creatinine, and blood urea nitrogen (BUN) in *Sgpl1*$^{fl/fl}$ (n = 3), *Sgpl1*$^{rosa+fl/fl}$ (n = 4) and *Sgpl1*$^{rosa+fl/fl+Fasudil}$ (n = 4) mice. **(F-H)** Periodic-acid Schiff (PAS) staining *Sgpl1*$^{fl/fl}$, *Sgpl1*$^{rosa+fl/fl}$, and *Sgpl1*$^{rosa+fl/fl+Fasudil}$ mice. Scale bar = 100 µm. A more severe phenotype was observed only in *Sgpl1*$^{rosa+fl/fl}$ kidneys. **(I)** Glomerulosclerosis (GS%) in *Sgpl1*$^{rosa+fl/fl}$ (Control) and *Sgpl1*$^{rosa+fl/fl+Fasudil}$ treated mice (Fasudil) was determined by visual inspection of ≥ 50 glomeruli in both kidney of n=3 mice.

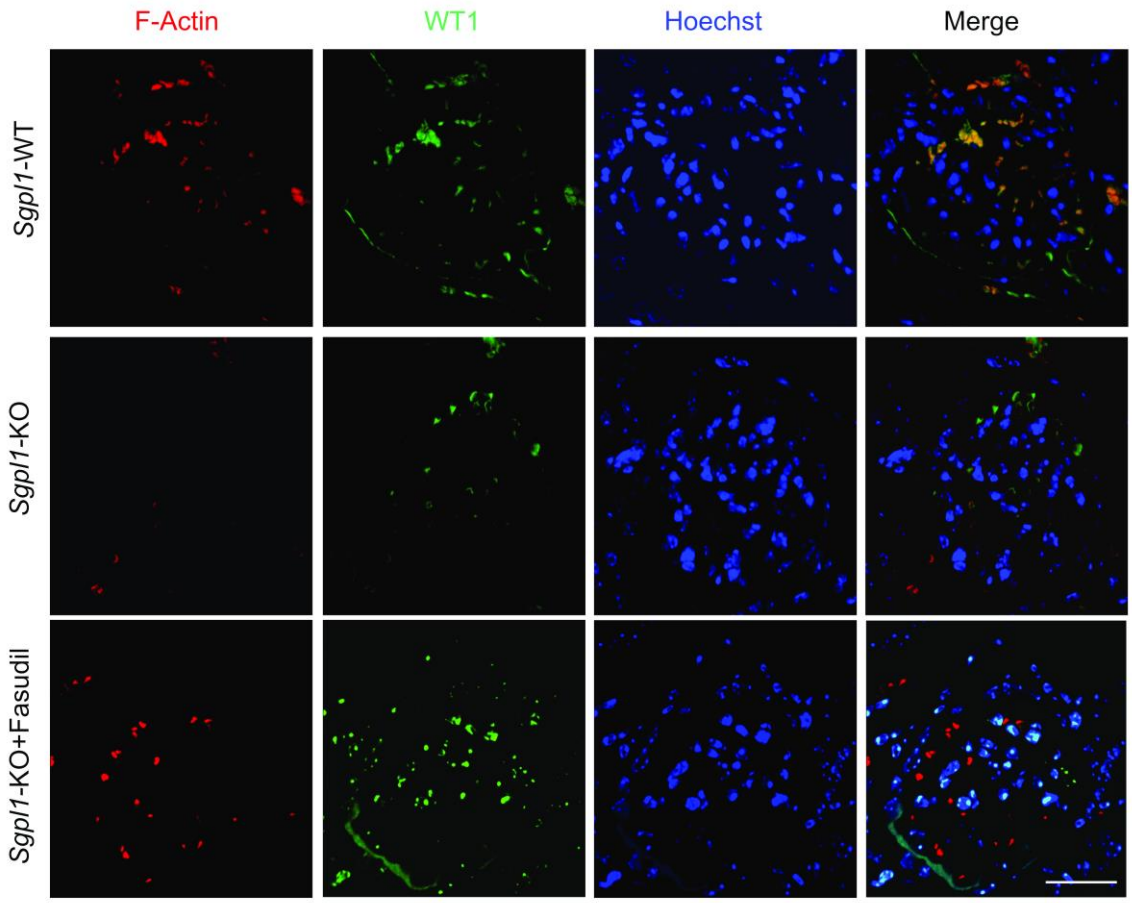

Figure 9: F-Actin and WT1 staining on kidneys of WT, *Sgpl1*-KO, and *Sgpl1*-KO treated with Fasudil. Phalloidin (red), WT1 (green), and DNA (blue) showing the presence of F-Actin (positive signals) in glomeruli of the WT and *Sgpl1*-KO treated with Fasudil, while a few signals of F-Actin were observed in *Sgpl1*-KO glomeruli. Scale bar = 1 mm.

Table 1 Clinical phenotypes of the SPLIS (p.Ser362Thr) patient

Findings and symptoms
Kidneys: • Congenital nephrotic syndrome • Anuric end-stage kidney disease*
Immune system: • T-cell deficiency and reduced number of B cells • Lymphopenia • Hypogammaglobulinemia • Recurrent viral and bacterial infections
Central nervous system: • Sensorineural hearing loss

• Two generalized seizures at the age of 8 weeks and 8 months • Computed tomography at the age of 8 months: slightly expanded cerebrospinal fluid spaces • Global developmental delay
Endocrinological system: • Adrenal insufficiency with recurrent episodes of arterial hypotension • Hypothyroidism
Lungs: • Recurrent respiratory tract infections with partial and global respiratory insufficiency • Chest computed tomography at the age of 9 months: interstitial lung disease
Electrolyte metabolism • Hypomagnesemia • Hypocalcemia
Additional findings • Poor feeding and failure to thrive • Thrombophilia with catheter-associated thromboses • Progressive decline in ultrafiltration in peritoneal dialysis